

Draft

DRAFT

Validation Problems for  
**3D NonLinear Analysis**  
of Reinforced Concrete Structures  
Using  
**MERLIN**

by

**Victor Saouma**

**Eric Hansen**

**Jan Červenka**

Department of Civil Engineering  
University of Colorado, Boulder



February 24, 2002

## Contents

<b>1</b>	<b>Introduction</b>	<b>3</b>
1.1	Objectives . . . . .	3
1.2	Computational Models . . . . .	3
<b>2</b>	<b>MERLIN Description</b>	<b>4</b>
2.1	Distributed Failure . . . . .	5
2.1.1	Smearred Cracks . . . . .	5
2.1.2	Concrete Crushing . . . . .	6
2.2	Localized Failure . . . . .	7
2.3	Algorithmic implementation . . . . .	11
<b>3</b>	<b>EDF Round-Robin Analyses</b>	<b>11</b>
3.1	Test A: Uniaxial Stress Cyclic Load . . . . .	11
3.1.1	Problem Description . . . . .	11
3.1.2	Results . . . . .	12
3.2	Test B: Rotation of Principal Stresses . . . . .	13
3.2.1	Problem Description . . . . .	13
3.2.2	Results . . . . .	13
3.3	Test C: Reinforced Concrete Beam . . . . .	16
3.3.1	Problem Description . . . . .	16
3.3.2	Results . . . . .	16
3.4	Test D: Mixed Mode Shear Failure . . . . .	18
3.4.1	Problem Description . . . . .	18
3.4.2	Results . . . . .	20
3.4.2.1	1a . . . . .	21
3.4.2.2	1b . . . . .	24
3.4.2.3	2a . . . . .	24
3.4.2.4	2b . . . . .	27
<b>4</b>	<b>San-Diego Column</b>	<b>27</b>
4.1	Problem Description . . . . .	27
4.2	Analysis . . . . .	27
<b>5</b>	<b>Conclusion</b>	<b>34</b>
<b>6</b>	<b>Acknowledgements</b>	<b>34</b>

## List of Figures

1	Merlin and Accompanying Programs . . . . .	4
2	Interface idealization and notations, (Cervenka, Chandra Kishen and Saouma 1998)	7
3	Interface Fracture, (Cervenka et al. 1998) . . . . .	8
4	Failure Function, (Cervenka et al. 1998) . . . . .	9
5	Bi-linear Softening Laws, (Cervenka et al. 1998) . . . . .	9
6	Stiffness Degradation in the Equivalent Uniaxial Case, (Cervenka et al. 1998) . . . . .	10
7	Configuration and Boundary Conditions for Tests A and B . . . . .	12
8	Load History for Test A . . . . .	12
9	Test A; Load Path . . . . .	15
10	Test A; (a) Normal Strain versus Normal Stress, (b) Normal Stress versus Volumetric Strain . . . . .	15
11	Test B; (a) Load Path, (b) Normal Strain versus Normal Stress . . . . .	16

12	Test B; (a) Transversal Strain versus Transversal Stress, (b) Shear Strain versus Shear Stress . . . . .	16
13	Test C Dimensions and Boundary Conditions . . . . .	17
14	Test C1; Boundary Description and FE (Surface) Mesh . . . . .	17
15	Test C1; Displacement Load Response . . . . .	18
16	Test C Steel Stresses . . . . .	19
17	Configuration of Tests D . . . . .	20
18	2D Automated Simulation of Crack Propagation in Tests D . . . . .	21
19	Simulation of Tests D . . . . .	22
20	Test D-1a; Load Path . . . . .	24
21	Test D-1a Final Deformed Shape . . . . .	27
22	Test D-1a; Normal Displacement versus Normal Load . . . . .	28
23	Test D-1b Final Deformed Shape . . . . .	28
24	Test D-1b; Normal Displacement versus Normal Load . . . . .	31
25	Test D-2a Final Deformed Shape . . . . .	32
26	Test D-2a; Normal Displacement versus Normal Load . . . . .	32
27	Test D-2b Final Deformed Shape . . . . .	33
28	Test D-2b; Normal Displacement versus Normal Load . . . . .	33
29	San-Diego Column R3; Dimensions . . . . .	35
30	San-Diego Column R3; Experimental Load-Displacement . . . . .	36
31	2D Analysis of the San-Diego Column, Increments 5 to 20 . . . . .	37
32	3D Analysis of San-Diego Column . . . . .	38
33	3D Analysis of San-Diego Column; Increments: 10, 20, 24, 44, 72, 96 . . . . .	38
34	2D and 3D Analysis of San-Diego Column; Smearred Cracks . . . . .	39
35	Load-Displacement Curves of the San-Diego Column Analysis . . . . .	40

## List of Tables

1	Test A: Specified Parameters . . . . .	11
2	Test A (Material Index 17) Control Data . . . . .	13
3	Test B Specified Parameters . . . . .	13
4	Load Increments for Test B . . . . .	14
5	Test B (Material Index 17) Control Data . . . . .	14
6	Test C Specified Parameters . . . . .	17
7	Test D Parameters . . . . .	19
8	Test D-1A (Material Index 1) Control Data . . . . .	23
9	Test D-1B (Material Index 1) Control Data . . . . .	25
10	Test D-2A (Material Index 1) Control Data . . . . .	26
11	Test D-2B (Material Index 1) Control Data . . . . .	29
12	Material Properties Used in Merlin . . . . .	30
13	Characteristics of the San-Diego Column Merlin Analysis . . . . .	31

## 1 Introduction

### 1.1 Objectives

The Research and Development division of *Electricité de France* (EDF) has recently organized a benchmark study of 3D concrete and reinforced concrete problems to assess various numerical models, (Ghavamian 2000). This report constitutes the results obtained by our group using the computer program MERLIN (Reich, Červenka and Saouma 1997).

Also included in this report, is a prior analysis of the, by now famous, “San-Diego” column which has been the subject of numerous analysis worldwide.

### 1.2 Computational Models

Nonlinear finite element modeling of (reinforced) concrete was the subject of much research 70’s and 80’s, mostly in association with the analysis of nuclear reactor vessel. At the time, most of the emphasis was on the modeling the compressive response of concrete based on plasticity models. Tensile response was, for the most part, handled by the smeared crack model first proposed by Rashid (1968). Most recently, there appear to have been on the one hand a decline in general interest in FE modeling of nuclear reactors, and on the other hand an explosion in research related to modeling concrete cracking.

Ever since the pioneering work of Bažant, Z.P. and Cedolin, L. (1979), there has been a recognition that: 1) unobjective results will be obtained if tensile stresses are merely limited to the tensile strength without adjustment for mesh size; and 2) concrete fails as a quasibrittle material, (Hillerborg, A. and Modéer, M. and Petersson, P.E. 1976). This in turn, has sparked much interest in the research community. The main challenge confronting the computational community has been how to localize a (smeared) crack in an objective manners, and if possible derive a “unified” constitutive model for tension and compression. This line of research has been most often presented at the FraM-CoS (Fracture Mechanics of Concrete Structures) conferences, (deBorst, Mazars, Pijaudier-Cabot and vanMier 2001). Some of the most recent and popular techniques include: Damage Mechanics, where the emphasis is on stiffness degradation rather than strength, (Mazars 1984); Microplane model, where the constitutive law is expressed in terms of stress and strain vectors rather than tensors, (Carol, Prat and Lopez 1997); Nonlocal continuum where the stress at a point depends on the strain history within a non-zero interaction radius; or combinations of the above (Hansen, Willam and Carol 2001). Most of these papers stem from a continuum mechanics/plasticity approach.

Invariably, most of the preceding papers begin with a statement indicating that whereas a discrete crack may be a more suitable model, its implementation (in the context of a non-linear analysis) would be too cumbersome to develop in light of the need to continuously remesh. As a result, some of the most innovative recent research have focused on alternate methods to model explicitly a discrete crack without remeshing, (Oliver, Huespe, Pulido and Chaves 2002), (Belytschko, T. and Moës and Usui, S. and Parimi, C. 2001), (Jirasek and Bažant 2001). These models are undoubtedly extremely powerful and promising, yet to the best of the author’s knowledge, none of them has yet been reported in a context other than a simplified linear elastic test problem. Their capability to handle “real-world” practical problems in the context of a full 3D, non-linear analysis (including multiple cracks, non-linear continuum, or cohesive stresses) remains to be proven.

Which brings us back to the discrete crack model. It is well known that this was the first one adopted in the pioneering work of Sims, Rhodes and Clough (1964) and Ngo and Scordelis (1967), but which was later dethroned by the smeared crack model of Rashid (1968), and the simplicity of its implementation as we were rapidly moving from the earlier linear elastic analysis to nonlinear ones, (Nilson 1968). The discrete crack model was revived by Saouma (1980), but its use has remained confined to the work at Cornell (where 3D problems appear to be addressed through a combination of linear finite and boundary elements) and the University of Colorado.

## 2 MERLIN Description

In general, a non-linear analysis of a reinforced concrete structure may consider the effects of plasticity, and/or damage (distributed failure), and/or fracture (localized, discrete failure).

MERLIN combines plasticity with fracture mechanics as two concurrent models. Plasticity-Continuum formulation is best suited to model distributed compressive failure, even through simple Drucker-Prager formulation. Its ability to model tensile failure, through a Rankine-type crack model, is adequate only if extensive cracking is present. On the other hand, a Fracture Mechanics-localized formulation is by far best suited to model individual cracks. This combination allows analyses of concrete structures which consider compressive failure (governed by plasticity), and both distributed failure (by smeared cracking) and localized failure (by fracture) under tension.

Hence, whereas the computational community is still searching for a “universal” model capable of correctly and efficiently predicting the non-linear response of reinforced concrete structures, an attempt is hereby made to combine different models into a single hybrid finite element code. Through this multi-faceted approach, we seek to adopt the right (but not necessarily the best) methodology for the right problem.

Merlin is a 3D static/dynamic finite element code supporting well over 20 different element types, 12 constitutive models, and various nonlinear algorithms. Originally developed for the fracture analysis of dams, it has recently been extended to include reinforced concrete. It supports both discrete cracks, (Cervenka et al. 1998) and smeared cracks (Hansen and Saouma 2002). Merlin was originally developed by Reich (1993), later extended by Červenka, J. (1994), and most recently updated and maintained by Cervenka, Hansen and Saouma.

Merlin is only one of a series of programs designed to facilitate its use. KumoNoSu, (Hansen and Saouma 2001) is a powerful 3D mesh generator built around the T3D code of (Rypl 1998) with an easy to use graphical user interface (which makes consultation of the Merlin Manual almost redundant). Spider (Hausman and Saouma 1998) is a 3D general purpose finite element postprocessor developed over the past 10 years by Hermanrud, Hausman and Saouma. RealView, developed by Hansen, enables the real time display of deformed mesh for each (time or load) increment while Merlin is running. Finally, Cracker, developed by Hansen, builds on the technology of Kumo to automate the process of (discrete) crack propagation. Whenever Merlin senses that a discrete crack needs to extend branch or nucleate (based on either LEFM or NLFM criterion), analysis is interrupted and control is passed to Cracker. This code in turns will modify the boundary description, generate a mesh and will then restart Merlin (for a full incremental analysis). Presently, the code is fully automated for 2D problems, extension to 3D is currently under development. Fig. 1 illustrates the interaction of the various codes.

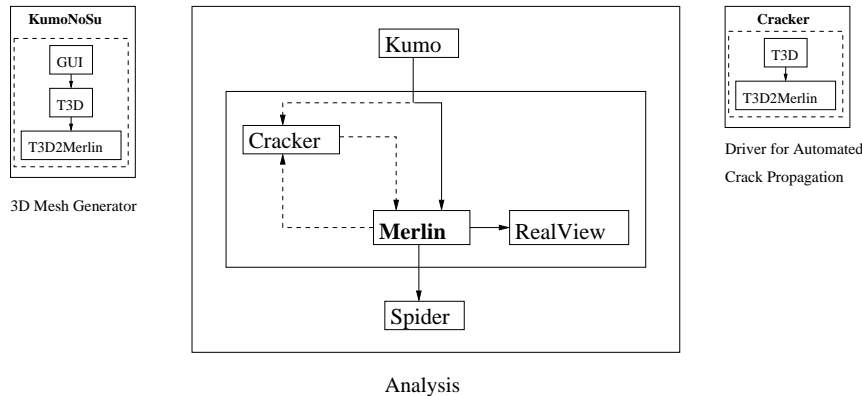


Figure 1: Merlin and Accompanying Programs

In the following sections, we shall examine each model separately.

## 2.1 Distributed Failure

Total strain can be decomposed into an elastic, plastic and fracture component.

$$\varepsilon_{ij} = \varepsilon_{ij}^e + \varepsilon_{ij}^p + \varepsilon_{ij}^f \quad (1)$$

thus new strain is determined from

$$\sigma_{ij}^n = \sigma_{ij}^{n-1} + E_{ijkl}(\Delta\varepsilon_{kl} + \Delta\varepsilon_{kl}^p + \Delta\varepsilon_{kl}^f) \quad (2)$$

### 2.1.1 Smeared Cracks

The smeared crack implementation is based on Rankine's failure criterion, exponential softening, with fixed or rotating cracks implemented within a crack band model through an orthotropic formulation.

Rankine's criteria for concrete cracking is given by

$$F_i^f = \sigma_{ii}^{tt} - f_{ti}' \leq 0 \quad (3)$$

where strains and stresses are expressed in material directions. For rotated cracks those correspond to the principal directions, and for the fixed crack model they correspond to the principal ones at the onset of first cracking.  $\sigma_{ii}^{tt}$  and  $f_{ti}'$  are thus the trial stress and tensile strength in the local material direction  $i$ .

Trial stress is determined from the elastic predictor

$$\sigma_{ij}^{tt} = \sigma_{ij}^{tn-1} + E_{ijkl}\Delta\varepsilon_{kl}' \quad (4)$$

If Equation 3 is violated (i.e. cracking occurs) then the incremental fracturing strain along direction  $i$  is such that the final strain must in turn satisfy

$$F_i^f = \sigma_{ii}^{tn} - f_{ti}' - E_{iikl}\Delta\varepsilon_{kl}' - f_{ti}' = 0 \quad (5)$$

Assuming that the increment of fracturing strain is normal to the failure surface, then for surface  $k$  the incremental fracturing strain is

$$\Delta\varepsilon_{ij}'^f = \Delta\lambda \frac{\partial F_k^f}{\partial \sigma_{ij}'} = \Delta\lambda \delta_{ik} \quad (6)$$

substituting, the incremental strain will thus be

$$\Delta\lambda = \frac{\sigma_{kk}^{tt} - f_{tk}'}{E_{kkkk}} = \frac{\sigma_{kk}^{tt} - f^{tt}(w_k^{max})}{E_{kkkk}} \quad (7)$$

where  $f^{tt}(w_k^{max})$  is the softening curve in terms of  $w$  which is the current crack opening. The softening diagram adopted in this model is the exponential decay function of (Hordijk 1991). The crack opening  $w$  is determined from

$$w_k^{max} = L_t(\hat{\varepsilon}_{kk}'^f + \Delta\lambda) \quad (8)$$

where  $\hat{\varepsilon}_{kk}'^f$  is the total fracturing strain in direction  $k$ , and  $L_t$  is the characteristic dimension of the element as introduced by (Bazant and Oh 1983). This dimension (or element) should be small enough to avoid numerical instabilities caused by potential material (stress-strain) snap-backs.

Distinction is made between the total maximum fracturing strain  $\hat{\varepsilon}_{kk}'^f$  and the current fracturing strain  $\varepsilon_{ij}'^f$  which is determined according to (Rots and Blaauwendraad 1989)

$$\varepsilon_{kl}'^f = (E_{ijkl} + E_{ijkl}')^{-1} E_{klmn} \varepsilon_{mn}' \quad (9)$$

$$\sigma_{ij}' = E_{ijkl}^{cr} \varepsilon_{kl}'^f \quad (10)$$

where  $E'_{ijkl}$  is the cracking stiffness in the local material (prime) direction. Assuming no interaction between normal and shear components

$$E'_{ijkl} = 0 \text{ for } i \neq k \text{ and } j \neq l \quad (11)$$

The mode I and II stiffnesses are then

$$E'_{iii} = \frac{f'^t(w_i^{max})}{\varepsilon'_{ii}} \quad (12)$$

$$E'_{ijij} = \frac{r_g^{ij}G}{1 - r_g^{ij}} \quad (13)$$

for  $i \neq j$ .  $r_g^{ij} = \min(r_g^i, r_g^j)$  is the minimum shear retention factors on cracks for the directions  $i$  and  $j$  and are given by (Kolmar 1986)

$$r_g^i = \frac{-\ln\left(\frac{\varepsilon'_{ii}}{c_1}\right)}{c_2} \quad (14)$$

$$c_1 = 7 + 333(\rho - 0.005) \quad (15)$$

$$c_2 = 10 - 167(\rho - 0.005) \quad (16)$$

where  $\rho$  is the reinforcement ratio assuming that it is below 0.002.  $G$  is the elastic shear modulus.

Finally, the secant constitutive matrix in the material direction is analogous to Eq. 9 as presented by (Rots and Blaauwendraad 1989)

$$\mathbf{E}'^s = \mathbf{E} - \mathbf{E}(\mathbf{E}'^{cr} + \mathbf{E})^{-1}\mathbf{E} \quad (17)$$

which should then be transformed to the global coordinate system  $\mathbf{E}^s = \Gamma_\varepsilon^T \mathbf{E}'^s \Gamma_\varepsilon$

## 2.1.2 Concrete Crushing

Adapted from (Cervenka and Červenka 1999)

Starting with the predictor-corrector formula, the stress is determined from

$$\sigma_{ij}^n = \sigma_{ij}^{n-1} + E_{ijkl}(\Delta\varepsilon_{kl} - \Delta\varepsilon_{kl}^p) = \sigma_{ij}^t - E_{ijkl}\Delta\varepsilon_{kl}^p = \sigma_{ij}^t - \sigma_{ij}^p \quad (18)$$

where  $\sigma_{ij}^t$  is the total stress, and  $\sigma_{ij}^p$  is determined from the yield function via the return mapping algorithm

$$F^p(\sigma_{ij}^t - \sigma_{ij}^p) = F^p(\sigma_{ij}^t - \Delta\lambda l_{ij}) \quad (19)$$

where  $l_{ij}$  is the return direction defined by

$$l_{ij} = E_{ijkl} \frac{\partial G^p(\sigma_{kl}^t)}{\partial \sigma_{kl}} \quad (20)$$

$$\Rightarrow \Delta\varepsilon_{ij}^p = \Delta\lambda \frac{\partial G^p(\sigma_{ij}^t)}{\partial \sigma_{ij}} \quad (21)$$

where  $G^p(\sigma_{ij})$  is the plastic potential function.

Two failure surfaces are considered:

**Drucker-Prager**, a two parameters model, (Drucker and Prager 1952), where the failure criteria is given by

$$F_{DP}^p = \alpha \mathbf{I}_1 + \sqrt{\mathbf{J}_2} - k = 0 \quad (22)$$

and  $\mathbf{I}_1$ , and  $\mathbf{J}_2$  are the first stress tensor invariant, and the second deviatoric stress tensor invariant respectively.  $\alpha$  and  $k$  are parameters controlling the surface.  $k$  controls the hardening/softening and is selected in such a way that the surface at the peak passes through the uniaxial compressive strength

$$k = k^0 \frac{f'_c(\varepsilon_{eq}^p)}{f'_c} \quad (23)$$

**Menétrey-Willam** a three parameters models, (Menétrey and Willam 1995) which provides more flexibility than the previous model

$$F_{MW}^P = \left[ \sqrt{1.5} \frac{\rho}{f'_c} \right]^2 + m \left[ \frac{\rho}{\sqrt{6} f'_c} r(\theta, e) + \frac{\xi}{\sqrt{3} f'_t} \right] - c = 0 \quad (24)$$

where

$$m = \sqrt{3} \frac{f'_c{}^2 - f'_t{}^2}{f'_c f'_t} \frac{e}{e+1} \quad (25)$$

$$r(\theta, e) = \frac{4(1-e^2) \cos^2 \theta + (2e-1)^2}{2(1-e^2) \cos \theta + (2e-1) \sqrt{4(1-e^2) \cos^2 \theta + 5e^2 - 4e}} \quad (26)$$

where  $(r, \xi, \theta)$  constitute the Heigh-Westerggard coordinates,  $f'_c$  and  $f'_t$  are the uniaxial compressive and tensile strength respectively. The curvature of the failure surface is controlled by  $e \in (0.5, 1.0)$  (sharp corner for  $e = 0.5$ , and circular for  $e = 1.0$ ). Failure surface depends on the strain hardening/softening parameter. For the Drucker-Prager model it depends on  $k$

$$k = k^0 \frac{f'_c(\varepsilon_{eq}^p)}{f'_c} \quad (27)$$

and for Menétrey Willam

$$c = \left( \frac{f'_c(\varepsilon_{eq}^p)}{f'_c} \right)^2 \quad (28)$$

where  $f'_c(\varepsilon_{eq}^p)$  is the hardening/softening law based on uniaxial test. The decending branch (softening) is defined in terms of stress displacements, and the equivalent plastic strain is transformed into displacements through length scale parameter  $L_c$ .

## 2.2 Localized Failure

Adapted from (Cervenka et al. 1998)

Contrary to the LEFM case, a nonlinear fracture mechanics model for a discrete crack between two homogeneous cementitious materials is not yet available. Hence, we first extend Hillerborg's model (Hillerborg, A. and Modéer, M. and Petersson, P.E. 1976) to account for mixed mode loading, and discuss its implementation within the context of a discrete crack model in a finite element code, (Červenka, J. 1994).

In the present model, the rock-concrete contact is idealized as an interface between two dissimilar materials with zero thickness. Thus, the objective is to define relationships between normal and tangential stresses with opening and sliding displacements. The notation used in the interface model is illustrated in Figure 2. The major premises upon which the model is developed are:

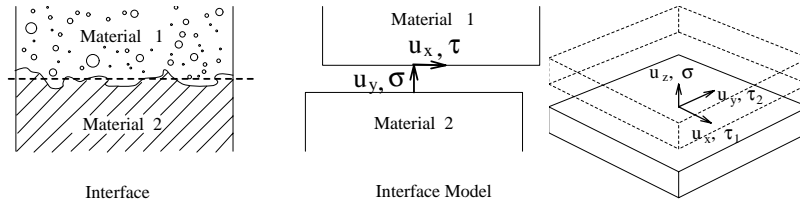


Figure 2: Interface idealization and notations, (Cervenka et al. 1998)

1. Shear strength depends on the normal stress.
2. Softening is present both in shear and tension.

3. There is a residual shear strength due to the friction along the interface, which depends on the compressive normal stress.
4. Reduction in strength, i.e. softening, is caused by crack formation.
5. There is a zero normal and shear stiffness when the interface is totally destroyed.
6. Under compressive normal stresses neither the shear nor the normal stiffnesses decrease to zero. In addition, should a compressive stress be introduced in the normal direction following a full crack opening, two faces of the interface come into contact, and both tangential and normal stiffnesses become nonzero.
7. Irreversible relative displacements are caused by broken segments of the interface material and by friction between the two crack surfaces.
8. Roughness of the interface causes opening displacements (i.e. dilatancy) when subjected to sliding displacements.
9. The dilatancy vanishes with increasing sliding or opening displacements.

Figure 3 illustrates the problem character of the fracturing process along an interface.

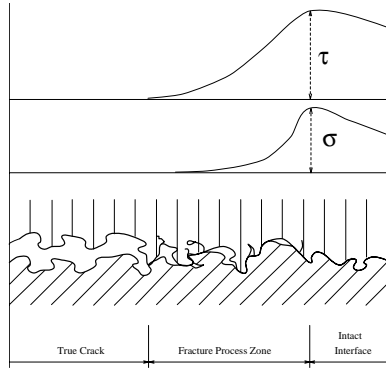


Figure 3: Interface Fracture, (Cervenka et al. 1998)

In the proposed model the strength of an interface is described by a failure function:

$$F = (\tau_1^2 + \tau_2^2) - 2c \tan(\phi_f)(\sigma_t - \sigma) - \tan^2(\phi_f)(\sigma^2 - \sigma_t^2) = 0 \quad (29)$$

where:  $c$  is the cohesion,  $\phi_f$  is the angle of friction,  $\sigma_t$  is the tensile strength of the interface,  $\tau_1$  and  $\tau_2$  are the two tangential components of the interface traction vector, and  $\sigma$  is the normal traction component.

The shape of the failure function in the two-dimensional case is shown in Figure 4, and it corresponds to the failure criterion first proposed by (Carol, I., Bažant, Z.P. and Prat, P.C., 1992). The general three-dimensional failure function is obtained by mere rotation around the  $\sigma$ -axis.

The evolution of the failure function is based on a softening parameter  $u^{\text{ieff}}$  which is the norm of the inelastic displacement vector  $\mathbf{u}^i$ . The inelastic displacement vector is obtained by decomposition of the displacement vector  $\mathbf{u}$  into an elastic part  $\mathbf{u}^e$  and an inelastic part  $\mathbf{u}^i$ . The inelastic part can subsequently be decomposed into plastic (i.e. irreversible) displacements  $\mathbf{u}^p$  and fracturing displacements  $\mathbf{u}^f$ . The plastic displacements are assumed to be caused by friction between crack surfaces and the fracturing displacements by the formation of microcracks.

$$\begin{aligned} F &= F(c, \sigma_t, \phi_f), \quad c = c(u^{\text{ieff}}), \quad \sigma_t = \sigma_t(u^{\text{ieff}}) \\ \mathbf{u} &= \mathbf{u}^e + \mathbf{u}^i, \quad \mathbf{u}^i = \mathbf{u}^p + \mathbf{u}^f \\ u^{\text{ieff}} &= \|\mathbf{u}^i\| = (u_x^i{}^2 + u_y^i{}^2 + u_z^i{}^2)^{1/2} \end{aligned} \quad (30)$$

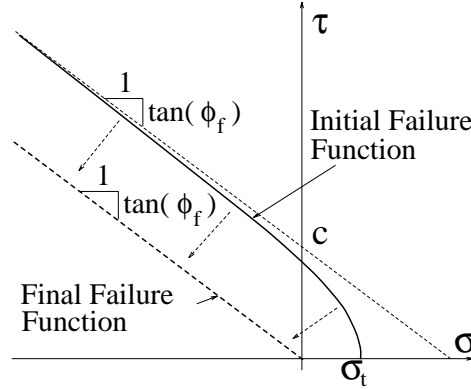


Figure 4: Failure Function, (Cervenka et al. 1998)

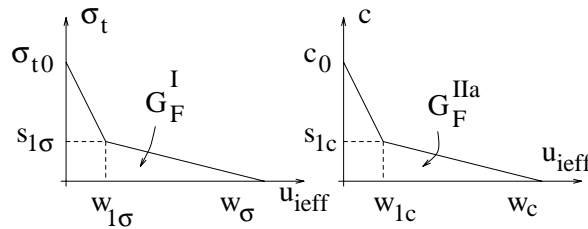


Figure 5: Bi-linear Softening Laws, (Cervenka et al. 1998)

In this work both linear and bilinear relationship are used for  $c(u^{\text{ieff}})$  and  $\sigma_t(u^{\text{ieff}})$ . in terms of  $G_F^I$  and  $G_F^{IIa}$  which are the mode I and II fracture energies, Fig. 5

It should be noted that  $G_F^{IIa}$  is not the pure mode II fracture energy (i.e. the area under a  $\tau$ - $u_x$  curve), but rather is the energy dissipated during a shear test with high confining normal stress. This parameter was first introduced by (Carol, I., Bažant, Z.P. and Prat, P.C., 1992) in their microplane model. This representation seems to be more favorable to the pure mode II fracture energy  $G_F^{II}$ . The determination of  $G_F^{II}$  would require a pure shear test without confinement, which is extremely difficult to perform. Alternatively, a  $G_F^{IIa}$  test requires a large normal confinement, and is therefore easier to accomplish. Furthermore, if  $G_F^{II}$  is used, the whole shear-compression region of the interface model would be an extrapolation from the observed behavior, whereas the second approach represents an interpolation between the upper bound  $G_F^{IIa}$  and the lower bound  $G_F^I$ .

The residual shear strength is obtained from the failure function by setting both  $c$  and  $\sigma_t$  equal to 0, which corresponds to the final shape of the failure function in Figure 4 and is given by:

$$\tau_1^2 + \tau_2^2 = \tan^2(\phi_f) \sigma^2 \quad (31)$$

Stiffness degradation is modeled through a damage parameter,  $D \in \langle 0, 1 \rangle$ , which is a relative measure of the fractured surface. Thus,  $D$  is related to the secant of the normal stiffness  $K_{ns}$  in the uniaxial case:

$$D = \frac{A_f}{A_o} = 1 - \frac{K_{ns}}{K_{no}} \quad (32)$$

where  $K_{no}$  is the initial normal stiffness of the interface;  $A_o$  and  $A_f$  are the total interface area and the fractured area respectively. It is assumed, that the damage parameter  $D$  can be determined by converting the mixed mode problem into an equivalent uniaxial one (Figure 6). In the equivalent uniaxial problem the normal inelastic displacement is set equal to  $u^{\text{ieff}}$ . Then, the secant normal stiffness can be determined from:

$$K_{ns} = \frac{\sigma}{u - u^p} = \frac{\sigma_t(u^{\text{ieff}})}{u^e + u^p + u^f - u^p} = \frac{\sigma_t(u^{\text{ieff}})}{\sigma_t(u^{\text{ieff}})/K_{no} + (1 - \gamma)u^{\text{ieff}}} \quad (33)$$

where  $\gamma$  is the ratio of irreversible inelastic normal displacement to the total value of inelastic displacement. Experimentally,  $\gamma$  can be determined from a pure mode I test through:

$$\gamma = \frac{u_p}{u_i} \quad (34)$$

where  $u^p$  is the residual displacement after unloading and  $u^i$  is the inelastic displacement before unloading. (Figure 6). For concrete,  $\gamma$  is usually assumed equal to 0.2 (Dahlblom and Ottosen 1990)

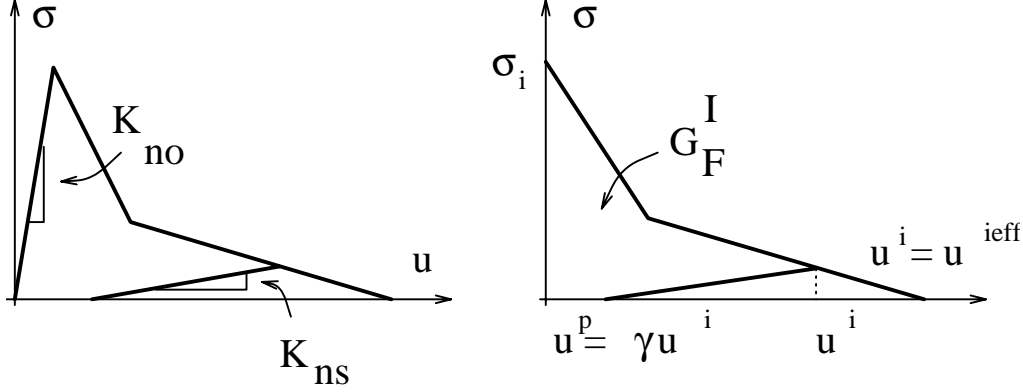


Figure 6: Stiffness Degradation in the Equivalent Uniaxial Case, (Cervenka et al. 1998)

or 0.3 (Alvaredo and Wittman 1992). Then, the evolution of the damage parameter  $D$  is defined by formula:

$$D = 1 - \frac{\sigma_t(u^{ieff})}{\sigma_t(u^{ieff}) + (1 - \gamma)u^{ieff}K_{no}} \quad (35)$$

which is obtained by substituting Equation 33 into Eq. 32.

The stress-displacement relationship of the interface is expressed as:

$$\boldsymbol{\sigma} = \alpha \mathbf{E}(\mathbf{u} - \mathbf{u}^p) \quad (36)$$

where: (a)  $\boldsymbol{\sigma}$  is the vector of tangential and normal stress at the interface.

$$\boldsymbol{\sigma} = \{\tau_1, \tau_2, \sigma\}^T \quad (37)$$

(b)  $\alpha$  is the integrity parameter defining the relative active area of the interface, and it is related to the damage parameter  $D$ .

$$\alpha = 1 - \frac{|\sigma| + \sigma}{2|\sigma|} D \quad (38)$$

It should be noted that  $\alpha$  can be different from 1 only if the normal stress  $\sigma$  is positive (i.e. the interface is in tension). In other words, the damage parameter  $D$  is activated only if the interface is in tension. In compression, the crack is assumed to be closed, and there is full contact between the two crack surfaces. The activation of  $D$  is controlled through the fraction  $\frac{|\sigma| + \sigma}{2|\sigma|}$ , which is equal to one if  $\sigma$  is positive, and is zero otherwise.

(c)  $\mathbf{E}$  is the elastic stiffness matrix of the interface.

$$\mathbf{E} = \begin{bmatrix} K_{to} & 0 & 0 \\ 0 & K_{to} & 0 \\ 0 & 0 & K_{no} \end{bmatrix} \quad (39)$$

It should be noted, that the off-diagonal terms in the elastic stiffness matrix  $\mathbf{E}$  of the interface are all equal to zero, which implies that no dilatancy is considered in the elastic range. The dilatancy is introduced later after the failure limit has been reached through the iterative solution process. The

dilatancy of the interface is given by dilatancy angle  $\phi_d$ , which is again assumed to be a function of  $u^{ieff}$ . In the proposed model, a linear relationship is assumed:

$$\begin{aligned} \phi_d(u^{ieff}) &= \phi_{d0} \left(1 - \frac{u^{ieff}}{u_{dil}}\right) & \forall u^{ieff} \leq u_{dil} \\ \phi_d(u^{ieff}) &= 0 & \forall u^{ieff} > u_{dil} \end{aligned} \quad (40)$$

where  $u_{dil}$  is the critical relative displacement after which, the interface does not exhibit the dilatancy effect any more, and  $\phi_{d0}$  is the initial value of the dilatancy angle.

## 2.3 Algorithmic implementation

Following the previous formulations for plasticity, smeared crack, and discrete cracking, a nonlinear analysis of a concrete structure combines three failure functions:

$$\begin{cases} \text{Smeared} & \begin{cases} \text{Plasticity} & F^p(\sigma_{ij}^{n-1} + E_{ijkl}(\Delta\varepsilon_{kl}^f - \Delta\varepsilon_{kl}^p)) \leq 0 \\ \text{Fracture} & F^f(\sigma_{ij}^{n-1} + E_{ijkl}(\Delta\varepsilon_{kl}^p - \Delta\varepsilon_{kl}^f)) \leq 0 \end{cases} \\ \text{Discrete} & F(\sigma_n + \mathbf{E}\Delta\mathbf{u}_n - \Delta\lambda\mathbf{E}\mathbf{m}, \mathbf{u}_i^{eff}) \leq 0 \end{cases} \quad (41)$$

Note that coupling only exists in the smeared crack model between the plasticity (Drucker-Prager or Menétrey-Willam) function and the Rankine smeared crack function. The complete smeared crack model and the discrete crack model remain uncoupled.

Solution of the smeared crack model involves the simultaneous solution of two failure functions, accomplished by:

1.  $F^p(\sigma_{ij}^{n-1} + E_{ijkl}(\Delta\varepsilon_{kl} - \Delta\varepsilon_{kl}^{f(i-1)} + b\Delta\varepsilon_{kl}^{cor(i-1)} - \Delta\varepsilon_{kl}^{p(i)})) \leq 0$ , solve for  $\Delta\varepsilon_{kl}^{p(i)}$
2.  $F^f(\sigma_{ij}^{n-1} + E_{ijkl}(\Delta\varepsilon_{kl} - \Delta\varepsilon_{kl}^{p(i-1)} - \Delta\varepsilon_{kl}^{f(i)})) \leq 0$ , solve for  $\Delta\varepsilon_{kl}^{f(i)}$
3.  $\Delta\varepsilon_{kl}^{cor(i)} = \Delta\varepsilon_{kl}^{f(i)} - \Delta\varepsilon_{kl}^{f(i-1)}$

where  $b$  is an iteration correction or relaxation factor which can accelerate convergence. As the discrete cracking formulation is separate from the smeared crack, it is solved independently.

## 3 EDF Round-Robin Analyses

### 3.1 Test A: Uniaxial Stress Cyclic Load

#### 3.1.1 Problem Description

This test seeks to determine the uniaxial response of a single linear four noded brick element subjected to a cyclic stress. Whereas the organizers sought the response of an assemblage of 1,000 elements (in order to effectively capture CPU time), we restricted ourselves to only one element. Fig. 7 illustrates the dimensions of the element, and Table 1 tabulates the prescribed material properties.

Elastic modulus $E$	32,000	MPa
Poisson coefficient $\nu$	0.2	
Maximum tensile stress $f'_t$	3	MPa
Maximum compressive stress $f'_c$	38.3	MPa
Maximum compressive strain $\varepsilon_c$	$2.0 \times 10^{-3}$	
Mode I Fracture Energy $G_F^I$	110	J/m <sup>2</sup>

Table 1: Test A: Specified Parameters

Load is to be applied as nodal displacements along the nodes, and each load sequence is to be applied through 50 increments. Load history is given by Fig. 8.

The following results are to be provided:  $\sigma_{xx} - \varepsilon_{xx}$ ,  $\sigma_{xx} - \varepsilon_{vol}$ , CPU time and memory allocation.

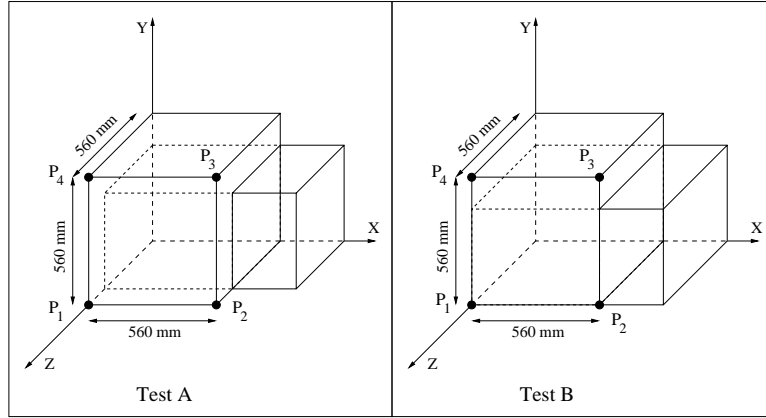


Figure 7: Configuration and Boundary Conditions for Tests A and B

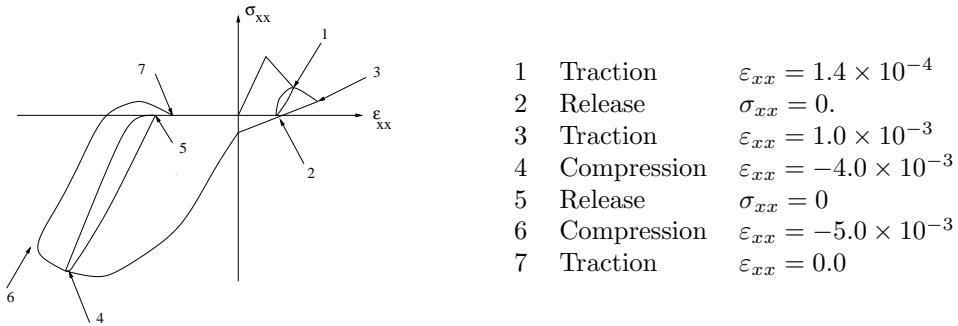


Figure 8: Load History for Test A

### 3.1.2 Results

MERLIN input data for this problem is given in Table 2. Fig. 9 illustrates the imposed axial strain history. Fig. 10(a) illustrates the normal stress versus normal strain, while Fig. 10(b) shows the normal stress versus volumetric strain results. The smeared crack/plasticity model applied to this problem considers non-linear behavior in tension due to material degradation represented by the smeared cracking model, while non-linear behavior in compression is due to plastic behavior. Given these constraints, the model performs quite well in this cyclic tension/compression test. Loading in tension occurs linearly up to the peak tensile strength  $f'_t$ , at which point elastic degradation due to smeared cracking causes softening. Unloading occurs at the current secant stiffness back to zero, at which point the material loads elastically in compression, with the stiffness recovery assumed to be due to the closing of the cracks opened during the tensile phase. Plasticity controls the response in the compression regime, and so the material undergoes non-linear hardening up to peak, followed by a more ductile softening response post-peak. Unloading in compression occurs at the elastic stiffness, following the guidelines of plasticity.

When compared with other submissions, MERLIN model fits quite well. The only apparent faults are the lack of some permanent displacement in the tensile direction (unloading somewhere between the elastic stiffness and the secant stiffness), and the lack of stiffness degradation in the compressive regime due to compressive cracking. However, considering the limitations of smeared cracking and plasticity theories to capture these respective phenomena, the response of the MERLIN analysis is reasonable.

Material Parameter	Values	Units
Modulus of elasticity $E$	32,000	MPa
Poisson's ratio $\nu$	0.2	
Tensile Strength	3.0	MPa
Fracture Energy	0.11	N/mm <sup>2</sup>
Compressive Strength	-38.3	MPa
Critical compressive displacement $w_d$	-5.0	mm
Return direction in Haig-Westergaard space $\beta$	0.	
Shape of Menetrey-Willam surface	0.55	
Onset of nonlinearity in compression $f_{c0}$	-24.0	MPa
Plastic strain at compressive strength	-0.00080	
Nonlinear Analysis Control Parameters		
Modified Newton-Raphson		
Number of Increments	350	
Maximum Number of Iterations	50	
Relative Residual Error Norm	0.05	
Absolute Residual Error Norm	0.1	
Displacement Error Norm	0.01	
CPU Time	9.9	sec.

Table 2: Test A (Material Index 17) Control Data

## 3.2 Test B: Rotation of Principal Stresses

### 3.2.1 Problem Description

This second test subjects a single brick element to a load history resulting in a continuously rotating orientation of the principal stresses.

The geometry, and boundary conditions are shown in Figure 7, and Table 3 tabulates the prescribed material properties.

Elastic modulus $E$	32,000	MPa
Poisson coefficient $\nu$	0.2	
Maximum tensile stress $f'_t$	3.0	MPa
Maximum compressive stress $f'_c$	38.3	MPa
Maximum compressive strain $\varepsilon_c$	$2.0 \times 10^{-3}$	
Mode I Fracture Energy $G_F^I$	110	J/m <sup>2</sup>

Table 3: Test B Specified Parameters

Two load increments are applied, Table 4. where  $\varepsilon_{xx}$ ,  $\varepsilon_{yy}$  and  $\varepsilon_{xy}$  are applied through nodes  $P_{2-x} - P_{3-x}$ ,  $P_{3-y} - P_{4-y}$  and  $P_{2-y} - P_{3-y}$  respectively. In the first loading path, node  $P_{2-y} = 0$  in order to ensure a homogeneous stress/strain behaviour. In the second load path,  $P_2$  will automatically be constrained to satisfy the prescribed value of  $\Delta\varepsilon_{xy}$ .

The following results are to be provided:  $\sigma_{xx} - \varepsilon_{xx}$ ,  $\sigma_{yy} - \varepsilon_{yy}$ ,  $\sigma_{xy} - \varepsilon_{xy}$ , CPU time and memory allocation.

### 3.2.2 Results

Again the Drucker-Prager/Rankine model of MERLIN was used, and the input data file is given by Table 5, the resulting load path by Fig. 11(a), and the single 3D element again by Fig. ??.

Results are illustrated by Fig. 11 to 12 which illustrate the normal, transversal and shear strains versus their corresponding stresses. The normal stress/strain plot of Fig. 11(b) shows a linear

	Increm.	
	1	2
$\Delta\varepsilon_{xx}$	1	0.5
$\Delta\varepsilon_{yy}$	$-\nu$	0.75
$\Delta\varepsilon_{xy}$	0	0.5

Table 4: Load Increments for Test B

Material Parameter	Values	Units
Modulus of elasticity $E$	32,000	MPa
Poisson's ratio $\nu$	0.2	
Tensile Strength	3.0	MPa
Fracture Energy	0.11	N-mm/mm <sup>2</sup>
Compressive Strength	-38.3	MPa
Critical compressive displacement $w_d$	-5.0	mm
Return direction in Haig-Westergaard space $\beta$	0.	
Shape of Menetrey-Willam surface	0.55	
Onset of nonlinearity in compression $f_{c0}$	-24.0	MPa
Plastic strain at compressive strength	-0.00080	
Nonlinear Analysis Control Parameters		
Modified Newton-Raphson		
Number of Increments	100	
Maximum Number of Iterations	100	
Relative Residual Error Norm	0.05	
Absolute Residual Error Norm	0.1	
Displacement Error Norm	0.01	
CPU Time	1.3	sec.

Table 5: Test B (Material Index 17) Control Data

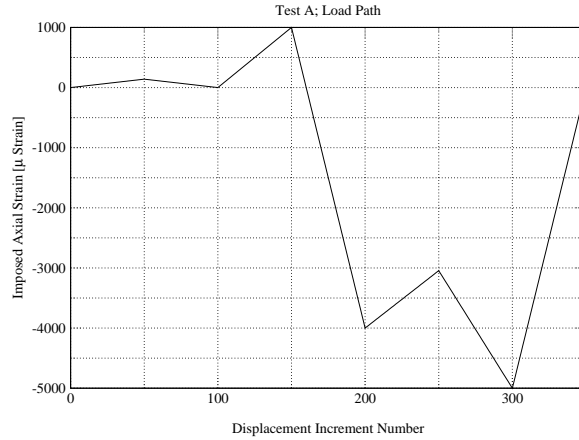


Figure 9: Test A; Load Path

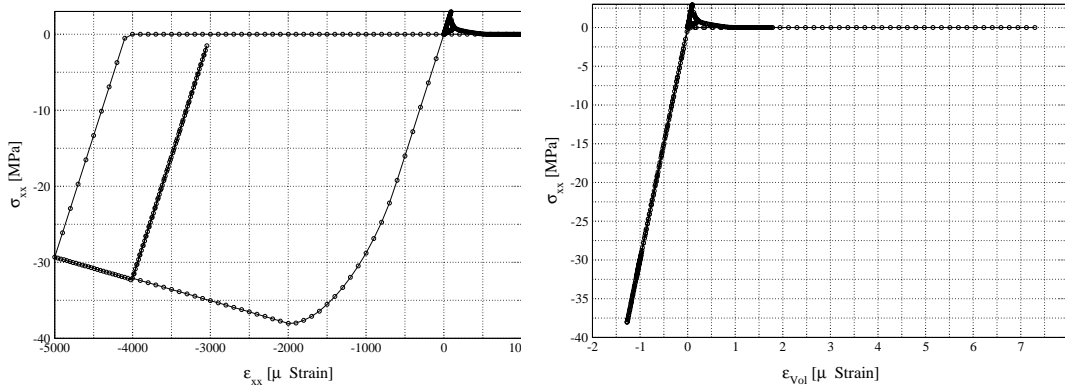


Figure 10: Test A; (a) Normal Strain versus Normal Stress, (b) Normal Stress versus Volumetric Strain

response up to the peak tensile strength  $f'_t$ , followed by rapid softening. However, the softening response in the post-peak regime is interrupted by a short plateau near the  $125.E - 6$  strain point. Past this plateau, softening continues down to the zero stress level. This plateau in the normal stress/strain response under the rotating principal stress loading scenario was also displayed by (Carol, Rizzi and Willam 2001) in the context of their “pseudo-Rankine” anisotropic damage formulation, and also by (Hansen 2000) in the context of his two-surface anisotropic damage/plasticity formulation. Hansen notes that the inflection point at the end of this stress plateau corresponds to a state of biaxial damage. In the case of the Rankine smeared crack model applied in this analysis, the normal stress plateau could also correspond to a state of distributed cracking in two orthogonal directions.

The transversal stress/strain plot of Fig. 12(a) also exhibits an initial linear response up to a peak stress below  $f'_t$ , followed by a rapid softening response down to zero stress. This lowered peak strength in the  $\sigma_{yy}$  direction is due to the cracking already present in the  $\sigma_{xx}$  direction. Similar results are shown in the  $\sigma_{xy}$  direction (Fig. 12(b)), with an initial linear response up to a lower shear strength (in comparison to  $\sigma_{xx}$  and  $\sigma_{yy}$ ), with the exception being the presence of another stress plateau in shear. At this plateau, the shear stress actually increases slightly before continuing to decrease down to zero.

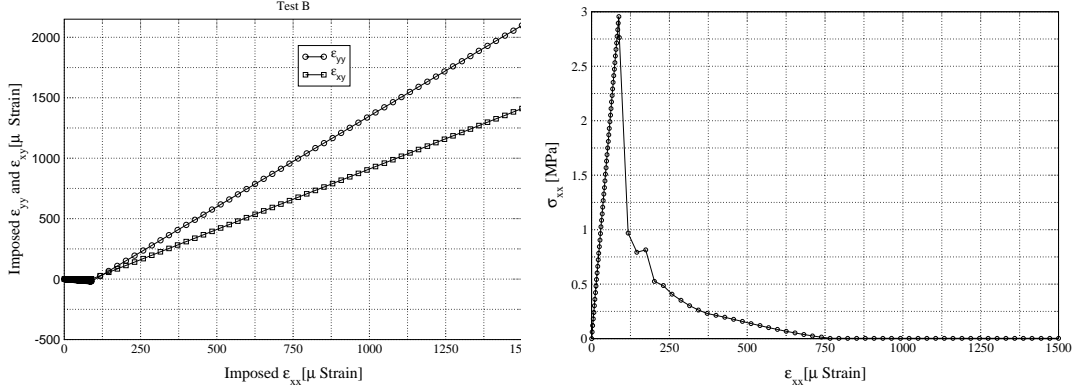


Figure 11: Test B; (a) Load Path, (b) Normal Strain versus Normal Stress

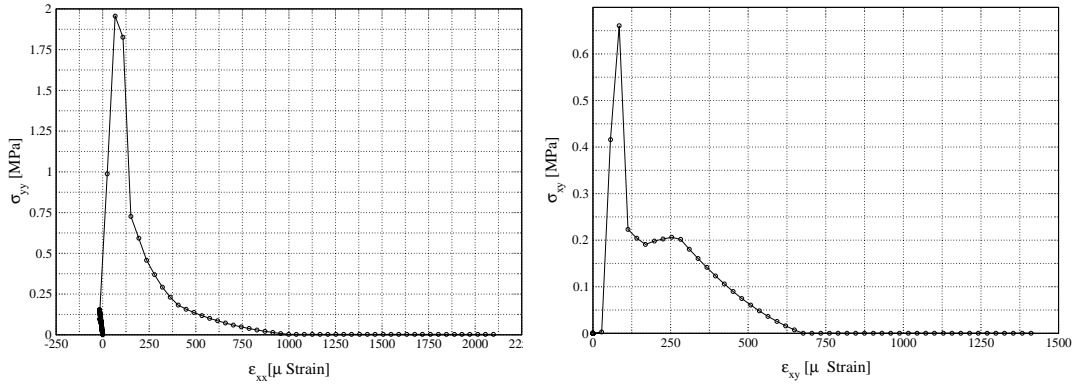


Figure 12: Test B; (a) Transversal Strain versus Transversal Stress, (b) Shear Strain versus Shear Stress

### 3.3 Test C: Reinforced Concrete Beam

#### 3.3.1 Problem Description

This third test seeks to assess the program capabilities in analyzing reinforced concrete structures. Two cases are considered, C1 and C2, without and with shear reinforcement respectively.

Fig. 13 illustrates the dimensions of the beam, and Table 6 tabulates the prescribed material properties.

The following results are to be provided: Load deflection curve (under applied load), central reinforcement strain history,  $\sigma_{xx}$  and  $\sigma_{xy}$  at span/4, concrete longitudinal stress and strain at  $z = 0$ ,  $y = -250$  mm, lower central steel longitudinal stress and strain history  $\sigma_{xx}(x, y)$  at  $z = 0$ , CPU time and memory allocation.

#### 3.3.2 Results

This problem was discretized, as all other ones, as a 3D problem in Merlin. The 3D finite element mesh for this problem (and the boundary description) are shown in Fig. 14. Three analyses were undertaken: 1) Linear continuum, single discrete crack (the single crack was justified by the point load); 2) Nonlinear continuum, no discrete crack; and 3) Nonlinear continuum and a single discrete crack. In all cases  $J_2$  plasticity was used for the reinforcement. The mesh for the first and third analyses had 1,263 nodes and 4,748 elements (including 28 interface elements), whereas the mesh

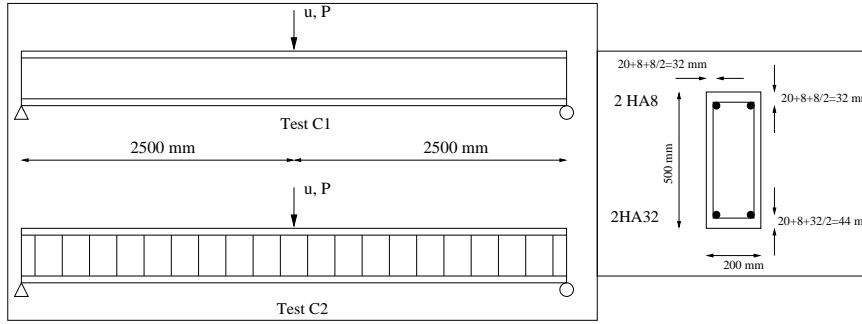


Figure 13: Test C Dimensions and Boundary Conditions

Concrete		
Elastic modulus $E$	37,272	MPa
Poisson's ratio $\nu$	0.2	
Maximum tensile stress $f'_t$	3.9	MPa
Maximum compressive stress $f'_c$	38.3	MPa
Maximum compressive strain $\varepsilon_c$	$2.0 \times 10^{-3}$	
Mode I Fracture Energy $G_F^1$	110	J/m <sup>2</sup>
Steel		
Elastic Modulus $E$	200,000	MPa
Poisson's ratio $\nu$	0.	
Yield Stress $f_y$	400	MPa
Plastic Tangent Stiffness $E_t$	3,245	MPa

Table 6: Test C Specified Parameters

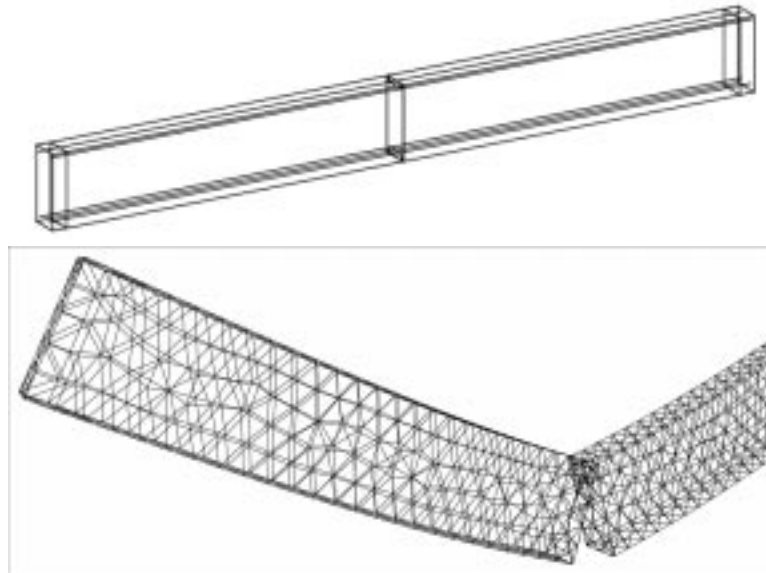


Figure 14: Test C1; Boundary Description and FE (Surface) Mesh

without discrete crack had 1,198 nodes and 4,729 elements. In all three cases 200 truss elements

were used  
Fig.

with

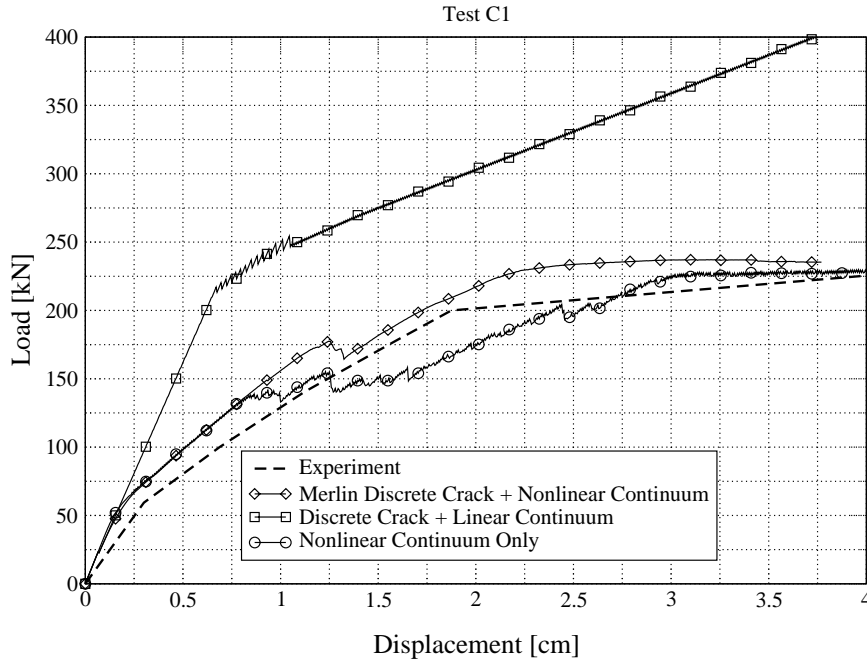


Figure 15: Test C1; Displacement Load Response

discrete crack (with ICM element) and linear continuum yields unacceptable results. On the other hand, whereas the analysis with nonlinear continuum is acceptable, it is not as good as the one based on our hybrid approach: discrete crack and nonlinear continuum. This last analysis yielded excellent results, it captured the cracking at 50 kN, prepeak continuous stiffness degradation, and finally the steel hardening up to 3.75 cm of imposed displacement (at which point the analysis was interrupted). However, it should be noted that the full nonlinearity (steel, continuum and crack) necessitated 14 hours of cpu.

Fig. 16 shows the stresses along the bottom steel in terms of displacement increments. It shows that the peak stress occurs at midspan, and the effect of hardening is well captured. The dip of steel stress at exactly midspan is the result of the discrete crack perturbation.

### 3.4 Test D: Mixed Mode Shear Failure

#### 3.4.1 Problem Description

This test, based on experiments reported in (B. 1992), seeks to determine the program's ability to handle shear and mixed-mode failure in concrete. The specimen is a double edge notch symmetrically loaded cube, Fig. 17.

The boundary conditions are such that the lower portion of the specimen is restrained along both the  $x$  and  $y$  displacements, tractions are applied on the top face and/or along the left side of the upper half through rigid steel plates.

Specified material properties are tabulated in Table 7. The following load paths must be considered:

**Path 1a: Tensile shear at zero axial load** The test specimen is first subject to the controlled displacement of  $A_3 - A_4$  until an average vertical displacement of  $\delta_n = 0.2$  mm is reached. Then the displacement decreases until the tensile force equals zero ( $P_n = 0$ ). Finally, an increasing

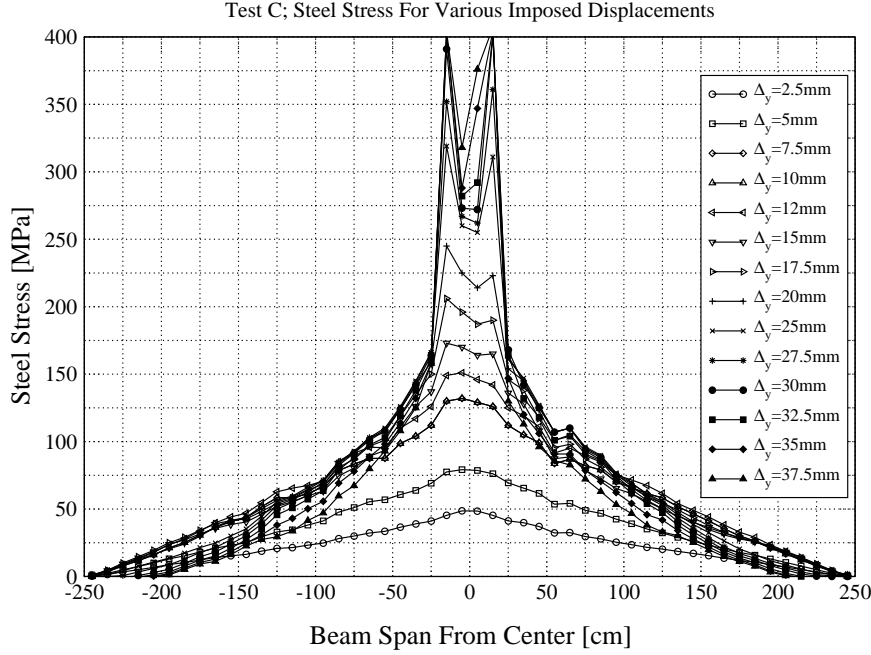


Figure 16: Test C Steel Stresses

Load Path 1a and 1b		
Elastic modulus $E$	32,800	MPa
Poisson coefficient $\nu$	0.2	
Maximum tensile stress $f'_t$	2.53	MPa
Maximum compressive stress $f'_c$	41.2	MPa
Maximum compressive strain $\epsilon_c$	$2.0 \times 10^{-3}$	
Mode I Fracture Energy $G_F^1$	110	J/m <sup>2</sup>
Maximum size aggregate $D_{agg}$	16	mm
Load Path 2a and 2b		
Elastic modulus $E$	32,800	MPa
Poisson coefficient $\nu$	0.2	
Maximum tensile stress $f'_t$	3.0	MPa
Maximum compressive stress $f'_c$	38.4	MPa
Maximum compressive strain $\epsilon_c$	$2.0 \times 10^{-3}$	
Mode I Fracture Energy $G_F^1$	110	J/m <sup>2</sup>
Maximum size aggregate $D_{agg}$	2	mm

Table 7: Test D Parameters

tensile shearing force  $P_s$  is applied until a displacement  $\delta_s$  of 0.15 mm is reached, whilst  $P_n$  is maintained at 0.

**Path 1b: Compressive shear at a constant axial confinement** The test specimen is first subjected to the controlled displacement of  $A_3 - A_4$  until an average vertical displacement of  $\delta_n = 0.2$  mm is reached. Then the displacement decreases until the compression force ( $P_n = -1$  kN) is reached. Finally, an increasing shearing force  $P_s$  is applied until a displacement of  $\delta_s = 0.15$  mm is attained, whilst  $P_n$  is maintained at  $-1$  kN.

**Path 2a: Axial tension at a constant compressive shear force of 5 kN** The test specimen

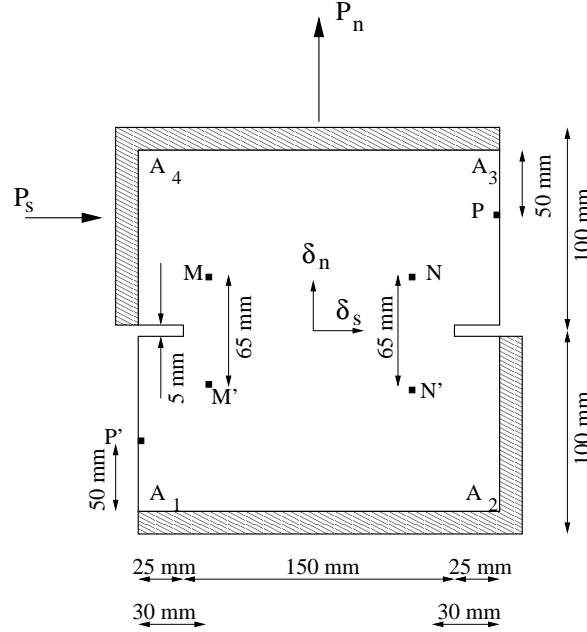


Figure 17: Configuration of Tests D

is first subject to shearing until the shearing force reaches  $P_s = 5$  kN (compressive shearing), whilst retaining  $P_n = 0$ . The shearing force is then maintained at a constant level and an increasing vertical displacement is applied until  $\delta_n = 0.15$  mm.

**Path 2b: Axial tension at a constant compressive shear force of 10 kN** The test specimen is first subject to shearing until the shearing force reaches  $P_s = 10$  kN (compressive shearing), whilst retaining  $P_n = 0$ . The shearing force is then maintained at a constant level and an increasing vertical displacement is applied until  $\delta_n = 0.15$  mm.

The following results are to be provided: Vertical load  $P_n$  vs vertical displacement  $\delta_n$ , shear load  $P_s$  vs transversal displacement  $\delta_s$ , vertical displacement  $\delta_n$  vs transversal displacement  $\delta_s$ , deformed mesh at end of each load path, CPU time, and memory allocation.

Note that the displacements are measured on the basis of the relative displacements between points  $M$ ,  $M'$ ,  $N$ ,  $N'$ ,  $P$  and  $P'$ . The shearing generated by  $\delta_s$  is measured at points  $P$  and  $P'$ , and the elongation or shortening in the  $\delta_n$  direction, within the cracked area, is obtained by calculating the average of the values measured between points  $M$  and  $M'$  and between  $N$  and  $N'$ :

$$\delta_s = \delta_s^P - \delta_s^{P'} \delta_n = (\delta_n^M - \delta_n^{M'} + \delta_n^N - \delta_n^{N'})/2 \quad (42)$$

### 3.4.2 Results

Analysis with Merlin were conducted in two steps. First a 2D analysis with a short initial notch was analysed. Merlin (in conjunction with its companion program Cracker) performed a 2D analysis in which a discrete crack propagation was automatically performed. The analysis proceeded as follows:

1. Perform a nonlinear incremental analysis of the specimen containing a short crack.
2. If during the analysis, it is determined that the stress at the tip of a crack exceeds the tensile strength, then, Fig. 18:
  - (a) Analysis is interrupted, and direction of crack propagation is passed by Merlin to Cracker.
  - (b) Cracker will automatically extend the mesh (by a user specified increment), and regenerate a finite element mesh.

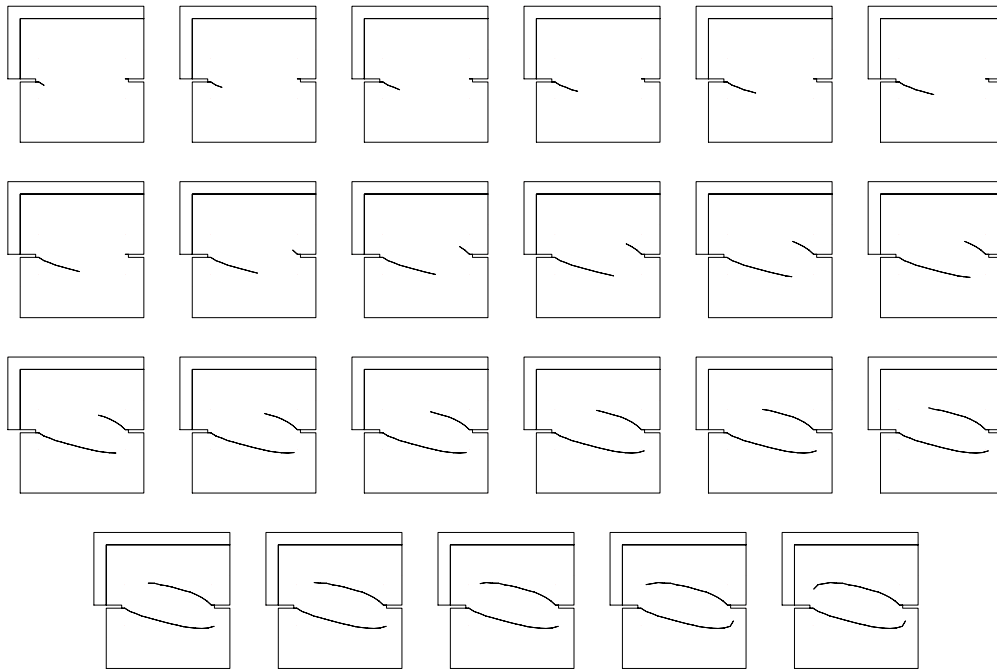


Figure 18: 2D Automated Simulation of Crack Propagation in Tests D

(c) Control is then transferred to Merlin which restarts the incremental analysis from zero following the remeshing.

3. Analysis will terminate under the following conditions:

- (a) The last load increment did not result in crack tip stresses exceeding the tensile strength.
- (b) Crack reaches a surface.

It should be noted that this process is now fully automated in 2D, work is under progress for 3D.

Hence, the analyses for test D was conducted in two parts. First a 2D simulation was performed to obtain the crack trajectory. Upon completion of this analysis, and with the known crack trajectory, the 2D mesh was extruded to a 3D mesh. Finally, the 3D mesh was incrementally analysed with an initial (closed) discrete crack. As the analysis progressed, the crack was automatically “unzipped”, and the crack front progressed, Fig. 19.

### 3.4.2.1 1a MERLIN input data file is given by Table 8

In test D1a, the notched specimen was subjected to an increasing vertical displacement until  $\delta_n = 0.2$  mm, after which it was unloaded until the vertical tensile load was zero. Once the vertical load had decreased to zero, it was maintained at that level while a monotonically increasing lateral displacement was imposed up to the point where  $\delta_s = 0.15$  mm. These two load paths are illustrated in Fig. 20.

The deformed mesh, shown in Fig. 21 interestingly shows that under normal load, the crack extended horizontally first, and when shear was applied, then the cracks kinked accordingly.

The numerical response during the vertical loading stage compares quite favorably with the experimental response, 22. The peak tensile load was over-predicted somewhat by the numerical model, but was within a reasonable margin of error. The post-peak response was also predicted fairly reasonably, although it can be seen that at the peak vertical displacement, the fracture energy was completely exhausted in the finite element model, whereas in the experiment, there was still

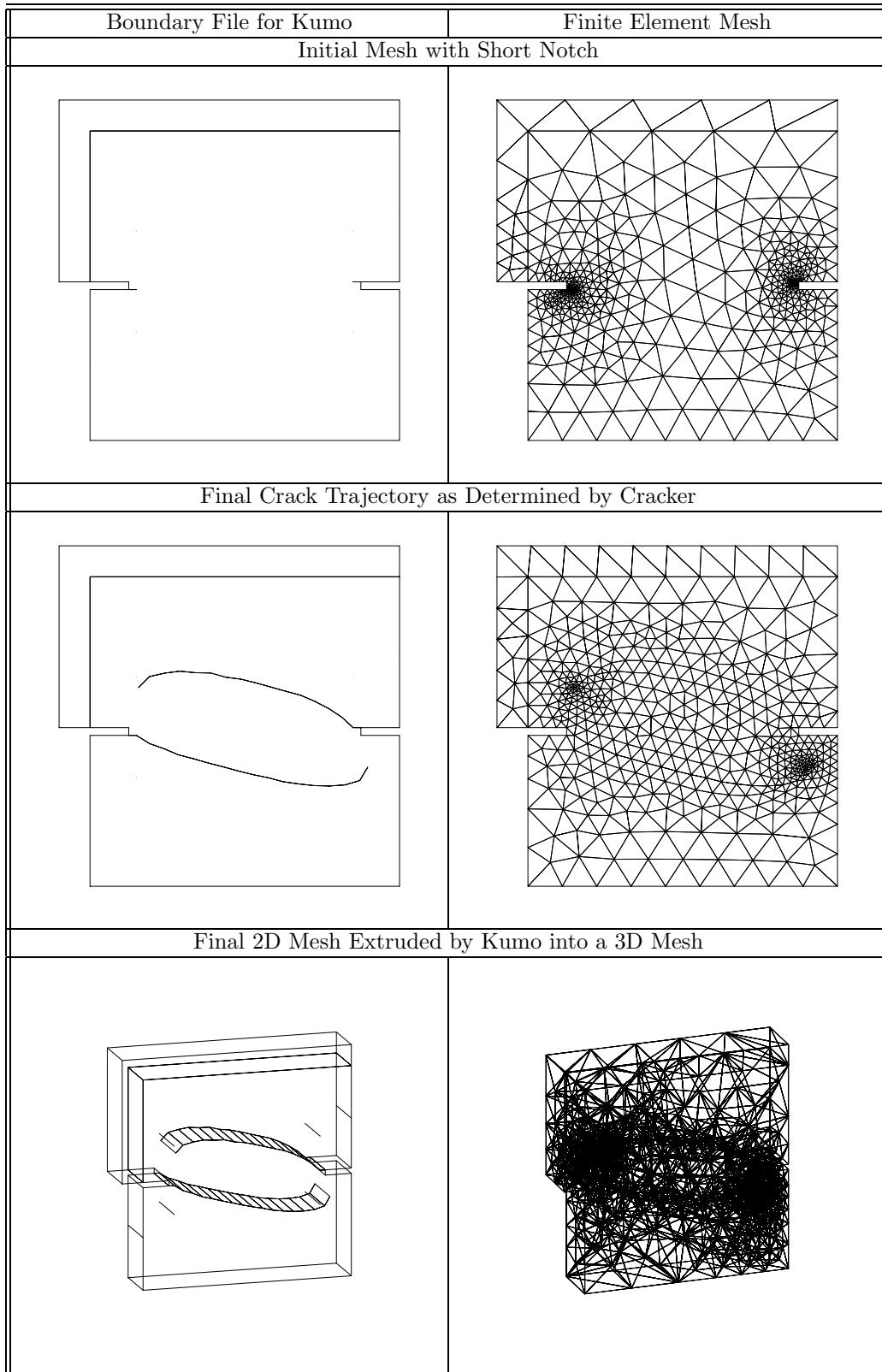


Figure 19: Simulation of Tests D

Material Parameter	Values	Units
Steel (Linear)		
Thickness	50	mm
Modulus of elasticity $E$	200,000	MPa
Poisson's ratio $\nu$	0.2	
Continuum Element (Linear)		
Thickness	50	mm
Modulus of elasticity $E$	32,000	MPa
Poisson's ratio $\nu$	0.2	
Interface Element (Non-linear)		
Shear stiffness $K_t$	3,280	MPa/mm
Normal stiffness $K_n$	3,280	MPa/mm
Tensile strength $f'_t$	2.53	MPa
Cohesion $c$	4.43	Mpa
Friction angle $\phi_f$	40.0	deg
Dilatancy angle $\phi_D$	10.0	deg
Specific mode I fracture energy $G_F^I$	0.11	MN-mm/mm <sup>2</sup>
Specific mode II fracture energy $G_F^{IIa}$	1.1	N-mm/mm <sup>2</sup>
Irreversible Deformation $\gamma$	0.3	
Maximal dilatant displacement $u_{dil}$	10	mm
Stress at break point of bilinear softening law $s_1$	0.633	MPa
Crack opening at break point of bilinear softening law $sw_1$	0.0326	mm
Cohesion at break point of bilinear softening law $c_1$	1.11	MPa
Crack sliding at break point of bilinear softening law $cw_1$	0.0186	mm
Nonlinear Analysis Control Parameters		
Number of Nodes	1,202	
Number of Elements	2,999	
Number of Increments	49	
Maximum Number of Iterations	2,000	
Energy Error Norm	1.0	
Relative Residual Error Norm	0.1	
Absolute Residual Error Norm	0.1	
Displacement Error Norm	0.001	
Nonlinear Algorithm	Tangent Stiffness; Line Search	
CPU Time	11.	min.

Table 8: Test D-1A (Material Index 1) Control Data

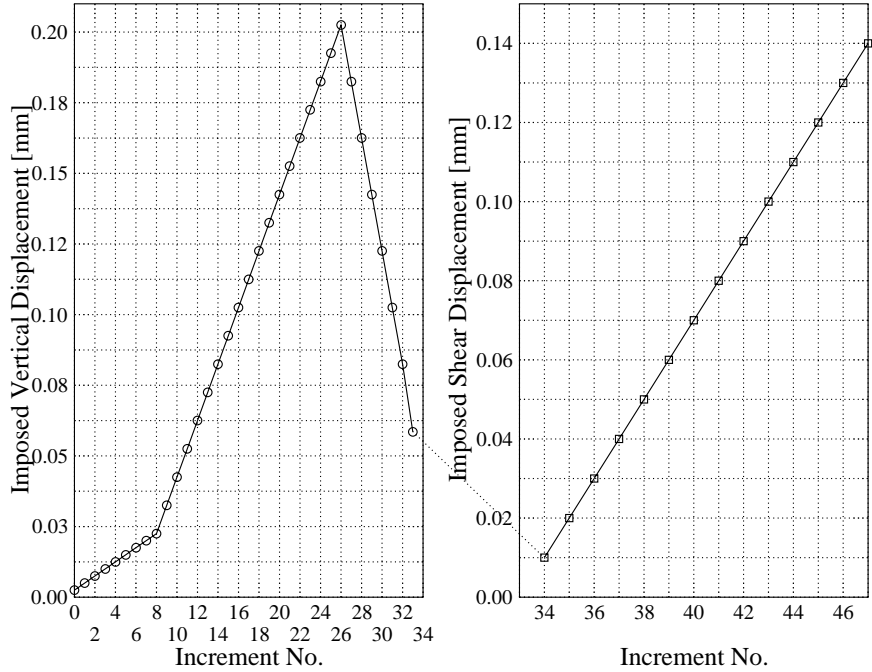


Figure 20: Test D-1a; Load Path

some residual strength left at that point. That is an indication that perhaps the concrete in the test specimen had a higher fracture energy than the value used in the numerical simulation.

**3.4.2.2 1b** For test 1b, MERLIN input data file is given by Table 9.

The loading pattern in test D-1b is quite similar to that of test D-1a, except that instead of simply reversing the vertical displacements until the vertical load equals zero, the loading continues until a vertical compressive load of 1 kN is applied. In addition, the shear displacements are in the “compressive” direction instead of the “tensile” direction of test D1a.

As with the preceding test, the crack first propagated colinearly under normal traction, and then curved due to shear, Fig. 23

As would be expected, the response during the vertical tensile loading phase (Fig. 24) is identical to that of test D1a (Fig. 22). The same is true of the vertical unloading, up to the point where the compressive load was applied.

Due to the friction generated by the vertical compressive load during shearing, significantly more shear resistance was realized in this test than in test D1a.

The load-displacement results in the normal direction again show good agreement with the experimental results, with just a slight over-estimation of the peak normal load  $P_n$  by the numerical simulation.

**3.4.2.3 2a** MERLIN input data file for test 2a is given by Table 10.

In contrast to the previous two tests, the specimen in test D2a was first subjected to shear (in the “compressive” direction) up to a shear load of 5 kN. Once that load was reached, a monotonically increasing vertical displacement was applied while the shear load of 5 kN was maintained.

Unlike the previous tests, where the specimens were first loaded in tension, the locations of the cracks could not be determined intuitively before the analysis.

The deformed mesh is shown in Fig. 25, and since the crack is entirely subjected to shear load, it curves immediately.

Load displacement curve for this test is shown in Fig. 26.

Material Parameter	Values	Units
Steel (Linear)		
Thickness	50	mm
Modulus of elasticity $E$	200,000	MPa
Poisson's ratio $\nu$	0.2	
Continuum Element (Linear)		
Thickness	50	mm
Modulus of elasticity $E$	32,000	MPa
Poisson's ratio $\nu$	0.2	
Interface Element (Non-linear)		
Shear stiffness $K_t$	3,280	MPa/mm
Normal stiffness $K_n$	3,280	MPa/mm
Tensile strength $f'_t$	2.53	MPa
Cohesion $c$	4.43	Mpa
Friction angle $\phi_f$ d1b-sn	10.0	deg
Dilatancy angle $\phi_D$	40.0	deg
Specific mode I fracture energy $G_F^I$	0.11	MN-mm/mm <sup>2</sup>
Specific mode II fracture energy $G_F^{IIa}$	1.1	N-mm/mm <sup>2</sup>
Irreversible Deformation $\gamma$	0.3	
Maximal dilatant displacement $u_{dil}$	10	mm
Stress at break point of bilinear softening law $s_1$	0.633	MPa
Crack opening at break point of bilinear softening law $sw_1$	0.0326	mm
Cohesion at break point of bilinear softening law $c_1$	1.11	MPa
Crack sliding at break point of bilinear softening law $cw_1$	0.0186	mm
Nonlinear Analysis Control Parameters		
Number of Nodes	1,231	
Number of Elements	3,588	
Number of Increments	48	
Maximum Number of Iterations	2,000	
Energy Error Norm	0.001	
Relative Residual Error Norm	0.1	
Absolute Residual Error Norm	0.1	
Displacement Error Norm	0.001	
Nonlinear Algorithm	Secant Newton; Line Search	
CPU Time	10.1	min.

Table 9: Test D-1B (Material Index 1) Control Data

Material Parameter	Values	Units
Steel (Linear)		
Thickness	50	mm
Modulus of elasticity $E$	$2. \times 10^9$	MPa
Poisson's ratio $\nu$	0.2	
Continuum Element (Linear)		
Thickness	50	mm
Modulus of elasticity $E$	32,000	MPa
Poisson's ratio $\nu$	0.2	
Interface Element (Non-linear)		
Shear stiffness $K_t$	3,280	MPa/mm
Normal stiffness $K_n$	3,280	MPa/mm
Tensile strength $f'_t$	3.0	MPa
Cohesion $c$	5.25	Mpa
Friction angle $\phi_f$	40.0	deg
Dilatancy angle $\phi_D$	10.0	deg
Specific mode I fracture energy $G_F^I$	0.11	MN-mm/mm <sup>2</sup>
Specific mode II fracture energy $G_F^{IIa}$	1.1	N-mm/mm <sup>2</sup>
Irreversible Deformation $\gamma$	0.3	
Maximal dilatant displacement $u_{dil}$	10	mm
Stress at break point of bilinear softening law $s_1$	0.75	MPa
Crack opening at break point of bilinear softening law $sw_1$	0.0275	mm
Cohesion at break point of bilinear softening law $c_1$	1.31	MPa
Crack sliding at break point of bilinear softening law $cw_1$	0.157	mm
Nonlinear Analysis Control Parameters		
Number of Nodes	926	
Number of Elements	2,153	
Number of Increments	50	
Maximum Number of Iterations	1,200	
Energy Error Norm	1.0	
Relative Residual Error Norm	0.1	
Absolute Residual Error Norm	0.1	
Displacement Error Norm	0.001	
Nonlinear Algorithm	Secant Newton; Line Search	
CPU Time	2.9	min.

Table 10: Test D-2A (Material Index 1) Control Data

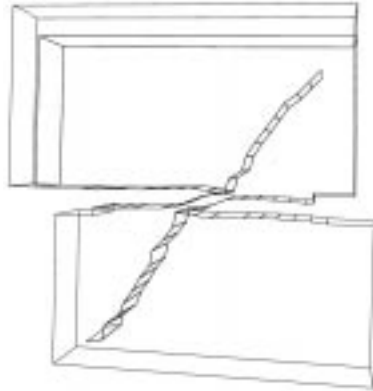


Figure 21: Test D-1a Final Deformed Shape

**3.4.2.4 2b** MERLIN input data file is given by Table 11.

The loading conditions for Test D2b are almost the same as those for Test D2a. The only difference between the two is that the specimen of Test D2b was loaded in shear up to 10 kN, instead of 5 kN, before the tensile loading phase, and then sustained during the normal loading phase.

The crack propagation is illustrated by Fig. 18. Interestingly we note that at first only the lower crack propagates, then the upper one, and finally both will propagate symmetrically, and the final deformed mesh is shown in Fig. 27.

Fig. 28 shows the load displacement curve. Pre-peak, peak and post-peak results are again relatively well captured.

## 4 San-Diego Column

### 4.1 Problem Description

The problem selected, is the R3 column tested by Xiao, Priestley and Seible (1993) and which has been the subject of numerous numerical simulation. Fig. 29 illustrates the column dimensions and reinforcement, and Fig. 30 the full load displacement curve of this column which was tested under cyclic load in load control. Undoubtedly, substantial damage (mostly debonding) is likely to have occurred prior to the application of the cycle with peak load, which resulted in a sudden and abrupt shear failure (accompanied by a substantial noise indicative of the brittleness of the failure). This resulted in a sudden drop in load, at that point, the load was reversed. The experimentally determined peak load of the column is 627 kN, while the theoretical flexural strength, and the one based on ACI-318 are 708 and 318 kN respectively. Undoubtedly, such a large discrepancy cries for a numerical simulation.

### 4.2 Analysis

The material properties adopted for this analysis are tabulated in Table 12.

Analyses, with displacement increments of 0.1 mm each, was performed on a Pentium II, 400 MHz PC, and details of the analysis are reported in Table 13.

Results for increments 5 to 20 of the 2D analysis, illustrating the evolution of the cracking is shown in Fig. 31.

Results of the 3D analysis are partially illustrated through Fig. 32, and 33.

Smearred cracks results for increment 19 for both 2D and 3D analysis are shown in Fig. 34.

Finally, all the load-displacement results are shown in Fig. 35. From these analyses, we conclude that:

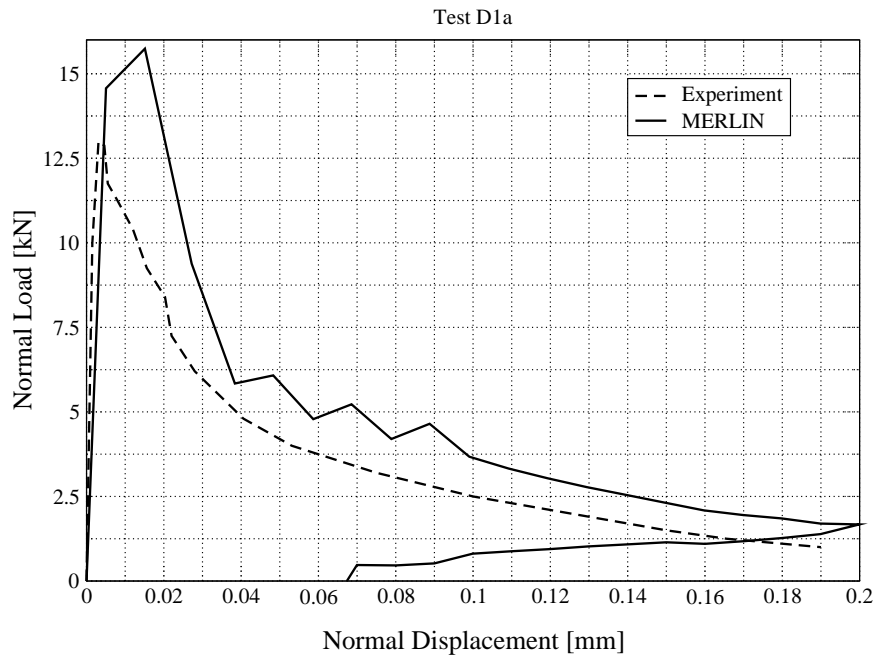


Figure 22: Test D-1a; Normal Displacement versus Normal Load

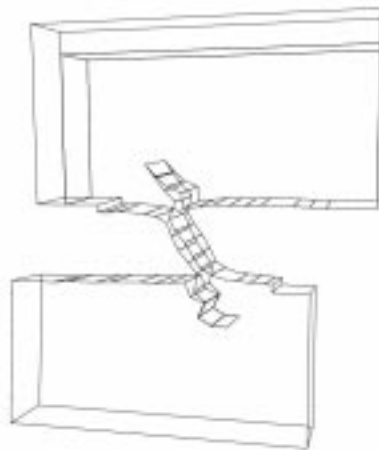


Figure 23: Test D-1b Final Deformed Shape

Material Parameter	Values	Units
Steel (Linear)		
Thickness	50	mm
Modulus of elasticity $E$	$2. \times 10^9$	MPa
Poisson's ratio $\nu$	0.2	
Continuum Element (Linear)		
Thickness	50	mm
Modulus of elasticity $E$	32,000	MPa
Poisson's ratio $\nu$	0.2	
Interface Element (Non-linear)		
Shear stiffness $K_t$	3,280	MPa/mm
Normal stiffness $K_n$	3,280	MPa/mm
Tensile strength $f_t'$	3.0	MPa
Cohesion $c$	5.25	Mpa
Friction angle $\phi_f$	40.0	deg
Dilatancy angle $\phi_D$	10.0	deg
Specific mode I fracture energy $G_F^I$	0.11	MN-mm/mm <sup>2</sup>
Specific mode II fracture energy $G_F^{IIa}$	1.1	N-mm/mm <sup>2</sup>
Irreversible Deformation $\gamma$	0.3	
Maximal dilatant displacement $u_{dil}$	10	mm
Stress at break point of bilinear softening law $s_1$	0.75	MPa
Crack opening at break point of bilinear softening law $sw_1$	0.0275	mm
Cohesion at break point of bilinear softening law $c_1$	1.31	MPa
Crack sliding at break point of bilinear softening law $cw_1$	0.157	mm
Nonlinear Analysis Control Parameters		
Number of Nodes	1,091	
Number of Elements	2,969	
Number of Increments	25	
Maximum Number of Iterations	1,200	
Energy Error Norm	1.0	
Relative Residual Error Norm	0.01	
Absolute Residual Error Norm	0.01	
Displacement Error Norm	0.001	
Nonlinear Algorithm	Secant Newton; Line Search	
CPU Time	2.0	min.

Table 11: Test D-2B (Material Index 1) Control Data

Units: Kg, mm, N. Hence Mpa ( $\text{N}/\text{mm}^2$ ).

<b>Mat. 1:</b> (Elem. 6, Mat. 15); Concrete			
$h$	410	mm	Thickness
$E$	27,761	MPa	Young's modulus
$\nu$	0.25		Poisson's ratio
$f'_c$	34.	MPa	Compressive Strength
$f'_t$	3.88	MPa	Tensile strength
$G_F$	0.1	N/mm	Fracture energy (arbitrarily selected)
$w_d$	0.5	mm	Compressive critical displacement
<b>Mat. 2:</b> (Elem. 23, Mat. 8); Interface crack			
$f'_c$	34	MPa	Compressive strength
$f'_t$	3.88	MPa	Tensile strength
$K_t$	300,000	MPa	10 times $E$
$K_n$	300,000	MPa	10 times $E$
$\Phi_F$	$40^\circ$		
$\Phi_D$	$20^\circ$		
$G_{IF}$	0.1	N/mm	Arbitrarily selected
$G_{IIF}$	1.	N/mm	10 times $G_{IF}$
$\gamma$	0.3		
$u_{D_{max}}$	10	mm	
$s_1$	0.97	MPa	$f'_t/4$
$w_1$	0.019	mm	$0.75 G_{IF}/f'_t$
$c$	6.8	MPa	Cohesion (check)
$c_1$	1.7	Pa	$c/4$
$cw_1$	0.11	m	$0.75 G_{IIF}/c$
<b>Mat. 3:</b> (Elem. 6 & 9, Mat. 1); Rigid/Elastic Concrete			
$h$	410.	mm	Thickness
$E$	50,000	MPa	Young's modulus
$\nu$	0.25		Poisson's ratio
<b>Mat. 4:</b> (Elem. 1, Group 4); Shear Reinf. Reinf.			
$A$	63.2	$\text{mm}^2$	Area
$E$	200,770	MPa	Young's modulus
$f_y$	317.	MPa	Yield stress
$H$	0.		Hardening modulus
<b>Mat. 5:</b> (Elem. 1, Group 4); Long. Reinf. (int.)			
$A$	567.7	$\text{mm}^2$	Area
$E$	200,770	MPa	Young's modulus
$f_y$	469.	MPa	Yield stress
$H$	0.		Hardening modulus
<b>Mat. 6:</b> (Elem. 1, Group 4); Long. Reinf. (ext.)			
$A$	1,425.8	$\text{mm}^2$	Area
$E$	200,770	MPa	Young's modulus
$f_y$	469.	MPa	Yield stress
$H$	0.		Hardening modulus

Table 12: Material Properties Used in Merlin

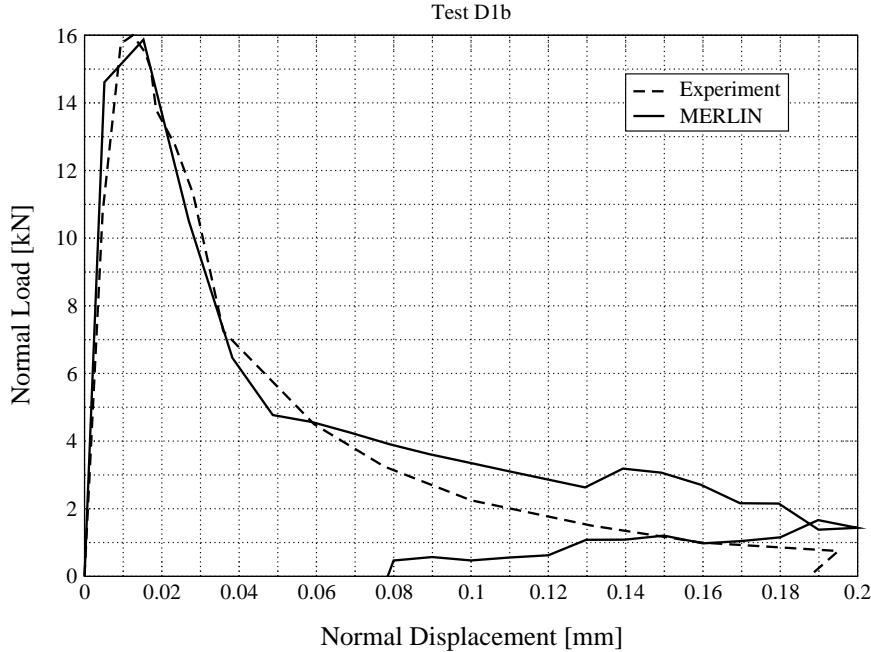


Figure 24: Test D-1b; Normal Displacement versus Normal Load

Anal.	Elem.	Nodes.	Max. Increm.	Error Norms				
				Iter.	Displ.	Abs. Resid.	Rel. Resid.	Time
2D	563	484	20	20	0.015	0.10	0.05	1 hr
3D	3,378	3,388	96	40	0.010	0.10	0.10	14 hrs

Table 13: Characteristics of the San-Diego Column Merlin Analysis

1. It is difficult to compare experimental results (with cyclic loads) with incremental single cycle analysis.
2. We capture substantial degradation and structural softening before the peak cycle.
3. The peak load is reasonably well predicted.
4. Brittle failure is captured through the sudden loss in load carrying capacity.
5. Brittle failure was captured primarily by the discrete crack.
6. Yielding plateau was predicted (not allowed to occur in the test), "makes sense".
7. 3D predictions slightly better than 2D.

Based on this analysis, we determined that improved results could be achieved should we modify Merlin to

1. Account for Bauschinger effect in steel
2. Account for hysteresis behavior for smeared and discrete cracks
3. Implement a more refined softening model (currently Hordijk, and Bilinear)
4. Recompute the tangent stiffness for the smeared cracks (material 15 and 16), rather than using the initial one.

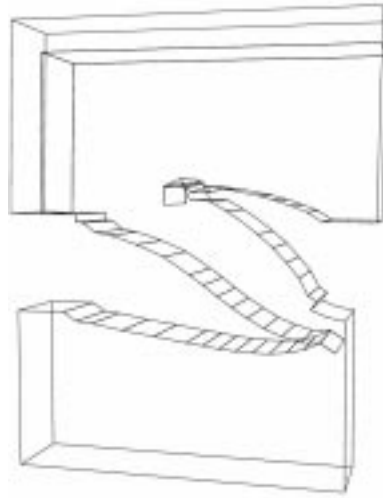


Figure 25: Test D-2a Final Deformed Shape

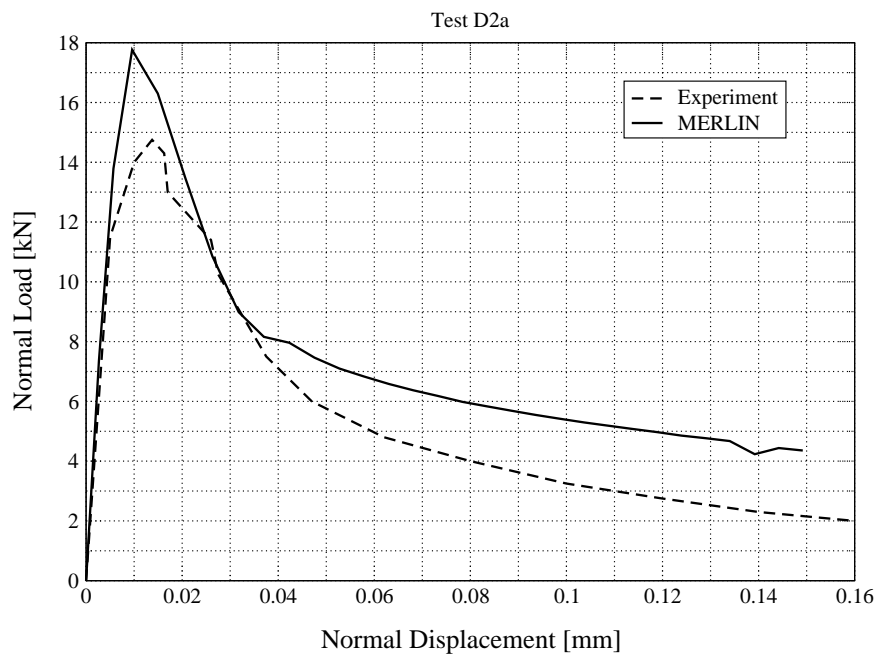


Figure 26: Test D-2a; Normal Displacement versus Normal Load

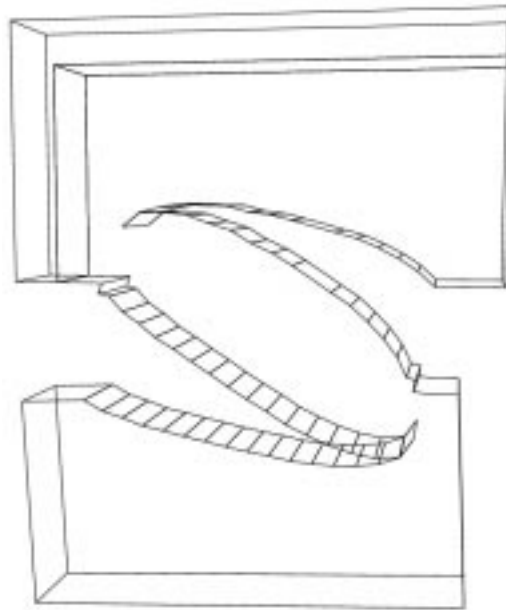


Figure 27: Test D-2b Final Deformed Shape

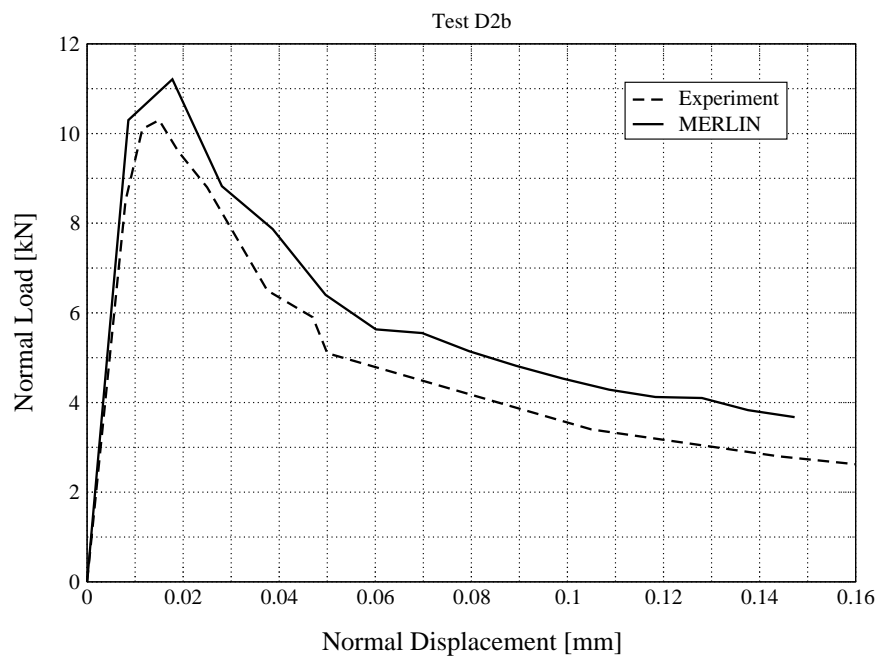


Figure 28: Test D-2b; Normal Displacement versus Normal Load

## 5 Conclusion

This report has proven the capabilities of MERLIN to combine discrete cracking, smeared cracking, and plasticity to model material nonlinearities in the context of a variety of loading scenarios prescribed by EDF. The capability to model discrete cracking through the use of interface elements and nonlinear fracture mechanics (NLFM) allows the simulation of localized cracks in a structure and their effects on the response of that structure. Smeared cracking allows models to capture the overall degradation of the strength and stiffness of a structure due to distributed cracking, and plasticity further complements the analysis capabilities by improving the response predictions of concrete under compressive loading and also the response of steel reinforcing bars. Together, these features allow MERLIN to accurately predict the responses of a variety of structures under various loading conditions.

## 6 Acknowledgements

The authors would like to thank, first and foremost, Dr. Jan Červenka for his continuous collaboration in the development of Merlin.

The development of MERLIN was originally supported by Mr. Doug Morris and the Electric Power Research Institute (EPRI). The authors would like to thank Mr. Uchita and the Tokyo Electric Power Company (TEPCO), and Mr. Shimpo and the Tokyo Electric Power Services Company (TEPSCO) for their current support of the extension of the capabilities of MERLIN. Further thanks to Dr. Daniel Ryppl (Ryppl 1998) for the adoption and use of his robust 3D mesh generator T3d.

Finally, Dr. Ben Spencer's is acknowledged for his analysis of EDF's test problems A and B (an initial unreported 2D analysis of tests D), as well for providing the initial mesh for the San-Diego column.

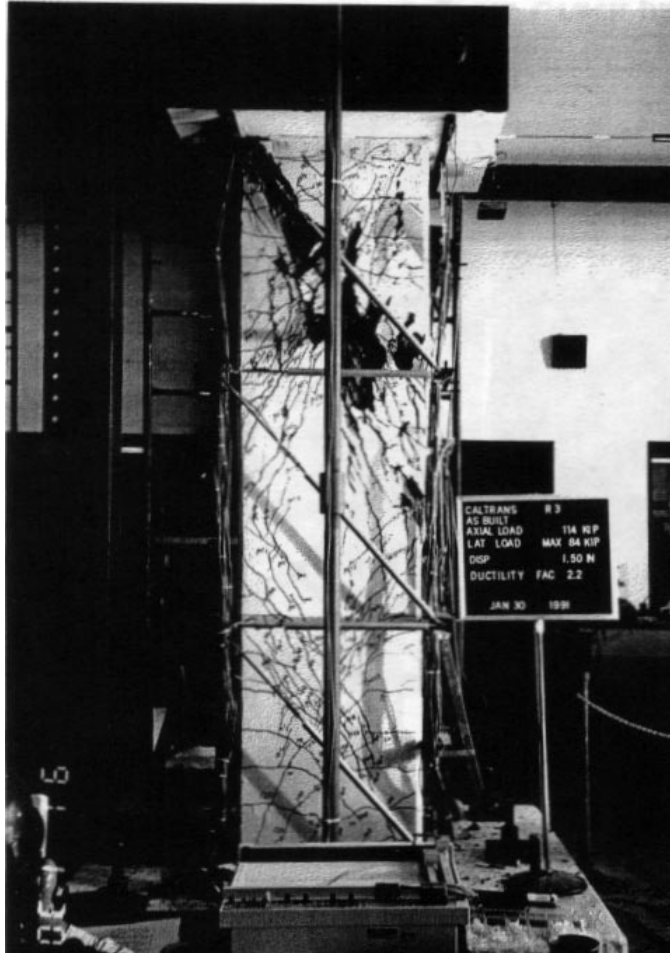
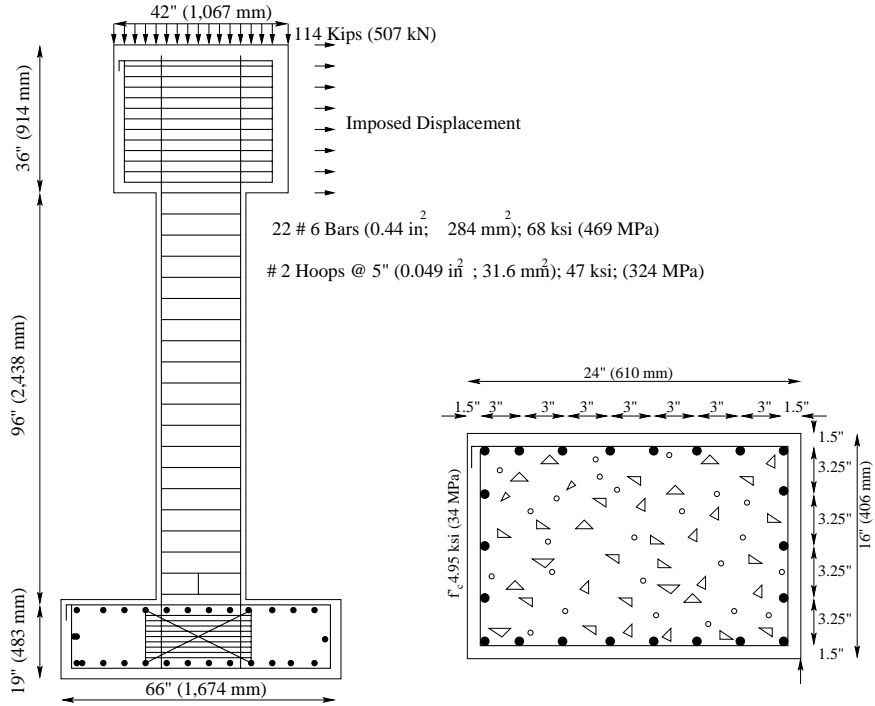


Figure 29: San-Diego Column R3; Dimensions

### Experimental Load–Displacement for Column R3 (Tested under Load Control)

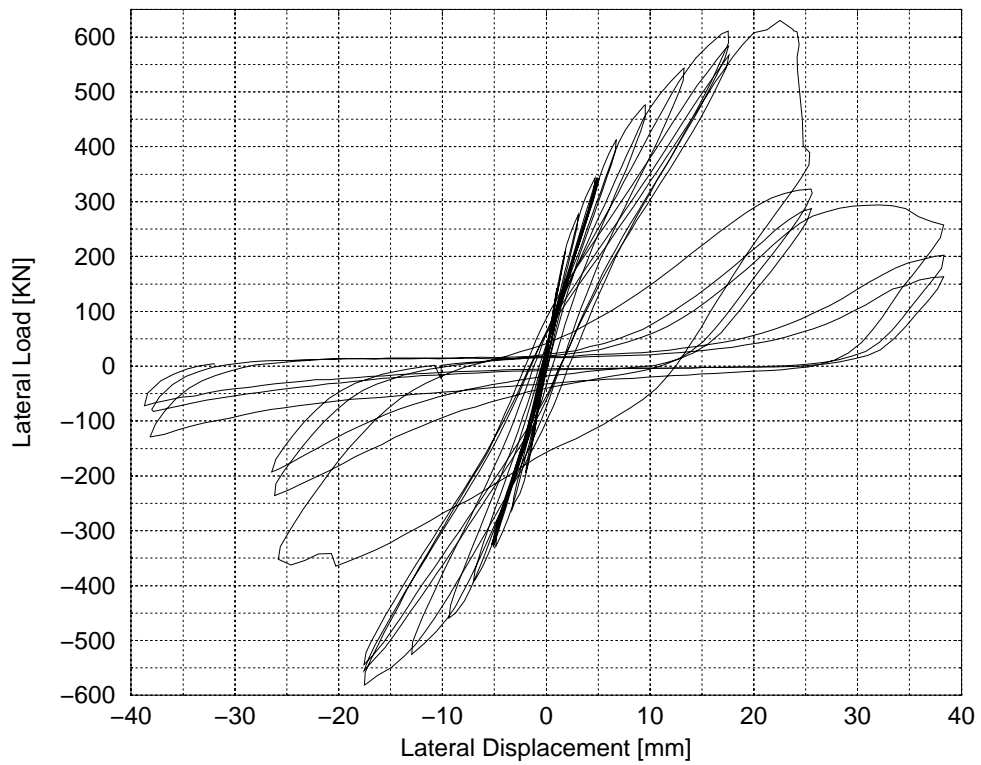


Figure 30: San-Diego Column R3; Experimental Load-Displacement

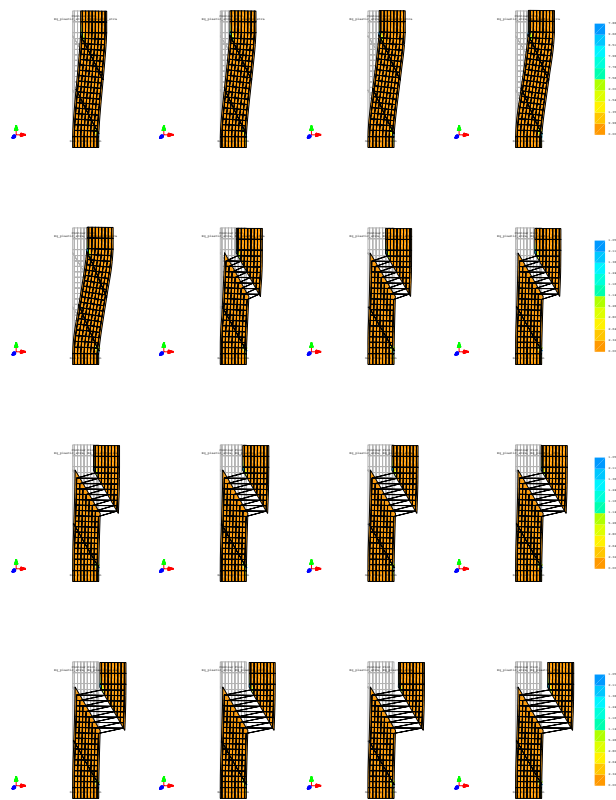


Figure 31: 2D Analysis of the San-Diego Column, Increments 5 to 20

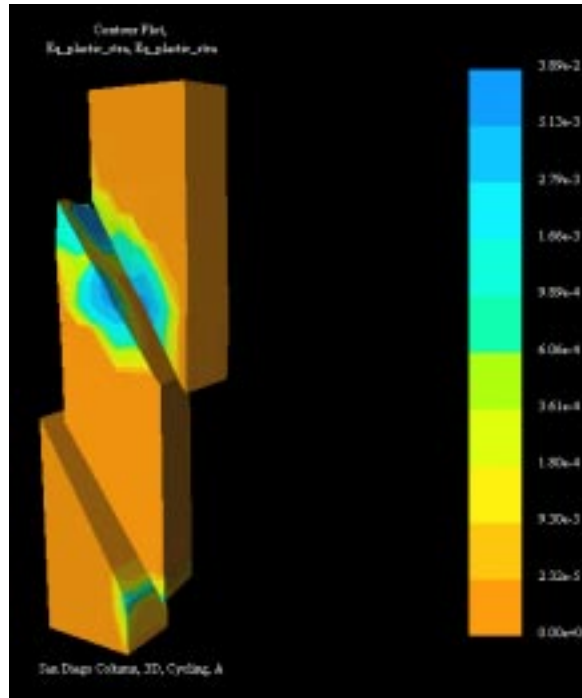


Figure 32: 3D Analysis of San-Diego Column

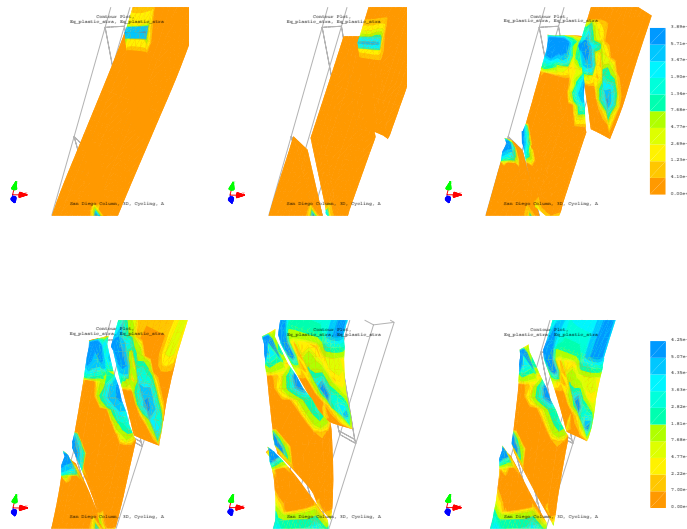


Figure 33: 3D Analysis of San-Diego Column; Increments: 10, 20, 24, 44, 72, 96

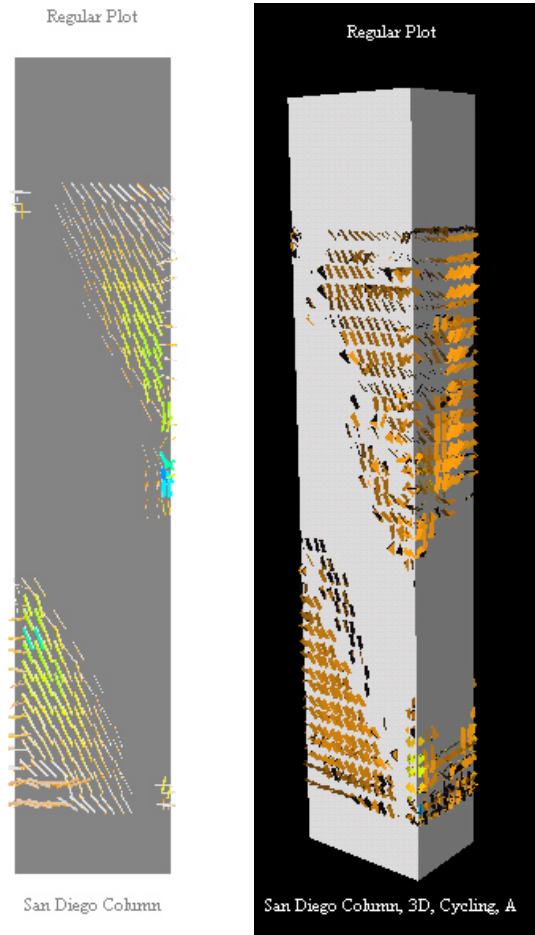


Figure 34: 2D and 3D Analysis of San-Diego Column; Smeared Cracks

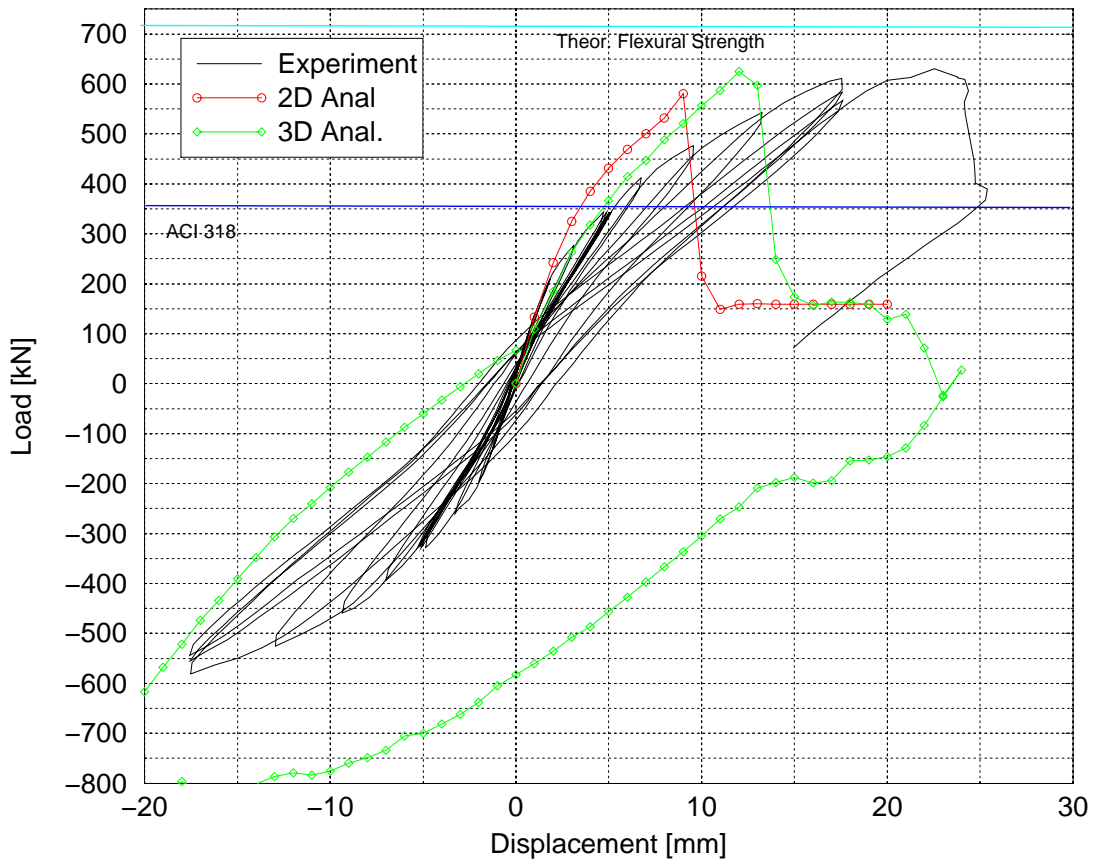


Figure 35: Load-Displacement Curves of the San-Diego Column Analysis

## References

- Alvaredo, A. and Wittman, F.: 1992, Crack formation due to hygral gradients, *Third International Workshop on Behaviour of Concrete Elements Under Thermal and Hygral Gradients*, Weimar, Germany.
- B., N.-M. M.: 1992, *Mixed-Mode Fracture of Concrete: an Experimental Approach*, PhD thesis, Delft University of Technology.
- Bažant, Z.P. and Cedolin, L.: 1979, Blunt crack propagation in finite element analysis, *J. of the Engineering Mechanics Division, ASCE* **105**, 297–315.
- Bazant, Z. and Oh, B.-H.: 1983, Crack band theory for fracture of concrete, *Materials and Structures* **16**, 155–177.
- Belytschko, T. and Moës and Usui, S. and Parimi, C.: 2001, Arbitrary discontinuities in finite elements, *Int. J. Numer. Meth. Engng* **50**, 991–1013.
- Carol, I., Bažant, Z.P. and Prat, P.C.: 1992, Microplane type constitutive models for distributed damage and localized cracking in concrete structures, *Proc. Fracture Mechanics of Concrete Structures*, Elsevier, Breckenridge, CO, pp. 299–304.
- Carol, I., Prat, P. and Lopez, C.: 1997, Normal/shear cracking model: Application to discrete crack analysis, *ASCE Journal of Engineering Mechanics*.
- Carol, I., Rizzi, E. and Willam, K.: 2001, On the formulation of anisotropic elastic degradation. part ii: Generalized pseudo-rankine model for tensile damage, *International Journal of Solids and Structures* **38**(4), 519–546.
- Cervenka, J. and Červenka, V.: 1999, Three dimensional combined fracture-plastic material model for concrete, *Journal of Mechanics of Frictional and Cohesive Materials*. In Print.
- Cervenka, J., Chandra Kishen, J. and Saouma, V.: 1998, Mixed mode fracture of cementitious bimaterial interfaces; part II: Numerical simulation, *Engineering Fracture Mechanics*.
- Dahlblom, O. and Ottosen, N. S.: 1990, Smearred crack analysis using a generalized fictitious crack model, *Journal of Engineering Mechanics* **116**(1), 55–76.
- deBorst, R., Mazars, J., Pijaudier-Cabot, G. and vanMier, J. (eds): 2001, Balkema Publishers.
- Drucker, D. and Prager, W.: 1952, Soil mechanics and plastic analysis of limit design, *Quarterly of Applied Mathematics* **10**(2), 157–165.
- Ghavamian, S.: 2000, Evaluation tests on models of non-linear behaviour of cracking concrete, using three dimensional modelling, *Technical Report CR 99-232*, EDF, Theroetical Mechanics and Applications R& D Division.
- Hansen, E.: 2000, *A two-surface anisotropic damage/plasticity model for plain concrete*, PhD thesis, University of Colorado at Boulder, Boulder, CO.
- Hansen, E. and Saouma, V.: 2001, Kumonosu, a 3d intereactive graphics mesh generator for merlin, *Technical report*, Report Submitted by the University of Colorado to the Tokyo Electric Power Service Company. <http://civil.colorado.edu/~saouma/Kumo>.
- Hansen, E. and Saouma, V.: 2002, Hibrid models for 3d reinforced concrete analysis, *Revue Francaise de Genie Civil*. In Print.
- Hansen, E., Willam, K. and Carol, I.: 2001, A two-surface anisotropic damage/plasticity model for plain concrete, in R. de Borst, J. Mazars, G. Pijaudier-Cabot and J. van Mier (eds), *Fracture Mechanics of Concrete Structures*, Balkema, Cachan.

- Haussman, G. and Saouma, V.: 1998, Spider, a 3d interactive graphics finite element post-processor, *Technical report*, Report Submitted by the University of Colorado to the Electric Power Research Institute, Palo Alto. <http://civil.colorado.edu/~saouma/Spider>.
- Hillerborg, A. and Modéer, M. and Petersson, P.E.: 1976, Analysis of crack formation and crack growth in concrete by means of fracture mechanics and finite elements, *Cement and Concrete Research* **6**(6), 773–782.
- Hordijk, D.: 1991, *Local approach to Fatigue of Concrete*, PhD thesis, Delft University of Technology.
- Jirasek, M. and Bažant, Z.: 2001, *Inelastic Analysis of Structures*, John Wiley, Chichester.
- Kolmar, W.: 1986, *Beschreibung der Kraftuebertragung ueber Risse in nichtlinearen Finite-Element-Berechnungen von Stahlbetontragwerken*, PhD thesis, Darmstadt.
- Mazars, J.: 1984, *Application de la Mécanique de L’Endommagement au Comportement Non Linéaire et a la Rupture du Béton de Structure*, PhD thesis, Ecole Normale Supérieure de l’Enseignement Technique, Université Pierre et Marie Curie, Cachan, France.
- Menétrey, P. and Willam, K.: 1995, Triaxial failure criterion for concrete and its generalization, *ACI Structural Journal* **92**(3), 311–318.
- Ngo, D. and Scordelis, A.: 1967, Finite element analysis of reinforced concrete beams, *Journal of the American Concrete Institute*.
- Nilson, A.: 1968, Nonlinear analysis of reinforced concrete by the finite element method, *Journal of the American Concrete Institute*.
- Oliver, J., Huespe, A., Pulido, M. and Chaves, E.: 2002, From continuum mechanics to fracture mechanics: The strong discontinuity approach, *Engineering Fracture Mechanics* **69**, 113–136.
- Rashid, Y.: 1968, Analysis of prestressed concrete pressure vessels, *Nuclear Engineering and Design*.
- Reich, R.: 1993, *On the Marriage of Mixed Finite Element Methods and Fracture Mechanics: An Application to Concrete Dams*, PhD thesis, University of Colorado, Boulder.
- Reich, R., Červenka, J. and Saouma, V.: 1997, Merlin, a three-dimensional finite element program based on a mixed-iterative solution strategy for problems in elasticity, plasticity, and linear and nonlinear fracture mechanics, *Technical report*, EPRI, Palo Alto. <http://civil.colorado.edu/~saouma/Merlin>.
- Rots, J. G. and Blaauwendraad, J.: 1989, Crack models for concrete: Discrete or smeared? fixed, multi-directional or rotating?, *HERON* **34**(1), 1512–1533.
- Rypl, D.: 1998, *Sequential and Parallel Generation of Unstructured 3D Meshes*, PhD thesis, Czech Technical University in Prague. <http://power2.fsv.cvut.cz/~sdr/t3d.html>.
- Saouma, V.: 1980, *Finite Element Analysis of Reinforced Concrete; a Fracture Mechanics Approach*, PhD thesis, Cornell University, Department of Structural Engineering.
- Sims, F., Rhodes, J. and Clough, R.: 1964, Cracking in norfolk dam, *J. of the American Concrete Institute*.
- Červenka, J.: 1994, *Discrete Crack Modeling in Concrete Structures*, PhD thesis, University of Colorado, Boulder.
- Xiao, Y., Priestley, M. and Seible, F.: 1993, Steel jacket retrofit for enhancing shear strength of short rectangular reinforced concrete columns, *Technical report*, Department of Applied Mechanics and Engineering Sciences, University of California at San Diego. Report Number SSRP-92/07.